1997

Design optimization of an interior permanent magnet motor

N. Sriram
University of Wollongong

DESIGN OPTIMIZATION OF AN INTERIOR PERMANENT MAGNET MOTOR

A thesis submitted in fulfilment of the requirements
for the award of the degree of

MASTER OF ENGINEERING (HONOURS)

from

UNIVERSITY OF WOLLONGONG

by

N. SRIRAM, B.E

School of Electrical, Computer and
Telecommunications Engineering
1997

Dedicated to

my parents and my sister

CONTENTS

ACKNOWLEDGEMENTS

I would like to express my deepest gratitude to Dr. B.S.P.Perera for his guidance and encouragement throughout the research. I am particularly indebted for the much required moral support and assistance provided by him during all stages of my research.

I would like to thank Professor C.D.Cook for his support in various ways especially during the early stages of my research. I wish to thank Mr. Phil Ciufo, for his timely help he had provided in the documentation of this thesis report. The workshop staff Mr. Joe Tiziano, Mr. Carlo Giusti, and Mr. Steve Petrou and the Professional Officer Mr. Peter Costigan have been most helpful and I wish to thank them for their co-operation and timely help. I would like to thank my friend Mr Ali Yazdian-Varjani for his encouragement and support to carry out my research successfully.

Finally, the financial support received from the Electricity Supply Association of Australia Limited and the Energy Research and Development Corporation (ESAA/ERDC) is greatly appreciated.

ABSTRACT

The work presented in this thesis is aimed at the design and optimization of an interior permanent magnet (IPM) synchronous motor. Emphasis is placed on reducing the quadrature axis inductance, by means of which better vector control and faster dynamics of the machine is achieved. The reduction in q-axis inductance is obtained by shaping the airgap. A general mathematical model for both the uniform and shaped airgap machines, having a hypothetical stator winding distribution is derived in this thesis. From the mathematical model, some of the important design parameters such as q-axis inductance and torque are calculated for the IPM machine. The mathematical models are then validated using finite element analysis.

The developed mathematical model is applied to two prototype machines each having different frame sizes. Calculated results from the application of the mathematical model to the prototype machines indicate that the q-axis inductance for the shaped airgap machine is reduced by about 45% when compared to the q-axis inductance of the uniform airgap machine. Calculated results from the finite element models applied to the existing prototype machine indicate that the q-axis inductance for the shaped airgap machine is reduced by about 41% when compared to the q-axis inductance of the uniform airgap machine. The percentage reduction between the shaped and uniform airgap machines, obtained from the application of finite element models to the 5.5kW prototype machine, is found to be equal to 33%. The difference in the percentage reduction between the finite element results in relation to the two prototype machines is attributed to the assumptions that are used in the winding distributions employed in the finite element models.

LIST OF SYMBOLS

B_a	Flux density in the airgap (T)
B_m	Flux density in the magnet (T)
B_p	maximum (peak) airgap flux density (T)
B_r	Residual flux density (T)
F	Magnetomotive force (A)
F_{mi}	MMF drop associated with the stator and rotor core (A)
g_a	Airgap length (m)
g_m	Thickness of the magnet (m)
g_{max}	Maximum length of the airgap (m)
g_{min}	Minimum length of the airgap (m)
H_a	Magnetic field intensity in the airgap (A/m)
H_c	Magnet coercivity (A/m)
H_m	Magnetic field intensity in magnet (A/m)
I	Rated current (A)
i_d	D-axis stator current (A)
i_q	Q-axis stator current (A)
K_w	Winding factor
L_d	D-axis stator inductance (H)
L_q	Q-axis stator inductance (H)
ℓ	Axial length of the machine (m)
N_p	peak number of turns

N_{ph}	Number of turns per phase
N_t	Total number of turns
P	Number of poles
r	Radius of the rotor (m)
T_t	Torque (Nm)
W	Width of the magnet (m)
λ_m	Magnet flux linkage (Wb)
ω_r	Rated speed (rad/sec)
θ	Electrical angle (deg)
μ_0	Permeability of free space (H/m)
θ_{re}	Reduced pole arc angle (deg)
ϕ	Flux (Wb)
φ_t	Total flux linkage (Wb)
δ	Electrical load angle (deg)

LIST OF FIGURES

CHAPTER 1

INTRODUCTION

1.1 Permanent magnet machines

Electric machines in which magnetic fields are produced by permanent magnets are called permanent magnet (PM) machines [1]. Permanent magnet motors are highly suitable for a wide variety of industrial applications, ranging from general purpose to high performance drives such as in robotics. The attractive power density and efficiency characteristics exhibited by these motors are major factors responsible for generating attention towards PM motors. PM motors also eliminate excitation losses that are commonly found in wound rotor motors. PM machines can be operated at higher power factors and can be designed to be mechanically reliable. The absence of slip rings is also a significant advantage over conventional wound rotor motors [2]. Rare-earth magnet materials such as Neodymium Iron Boron (Nd-Fe-B) has led to the development of PM motors having high torque to volume ratios thus enabling compact designs. The developments of vector control techniques have also made PM motors very attractive in their applications such as servo-drives for machine tools and robots.

1.2 Past studies on permanent magnet machines

Most of the past research on PM motors have been concentrated on studies such as the development of the rotor configurations, operating modes including the flux weakening mode, performance characteristics, including torque control and saturation effects and design optimization of the motor design using computer simulation to maximize the efficiency.

The aspects of relevance involved in the development of rotor configurations were the positioning of the magnets, the types of permanent magnet materials, robustness, simplicity of construction and optimum output. One of the early PM

motors developed by Merrill [3] has a rotor structure employing integral cast magnets or magnet blocks. This motor faced strong leakage flux problems from one pole to another through the outer ring of laminations. Honsinger [4] developed a rotor configuration by mounting the permanent magnets within the flux barrier of a conventional reluctance motor where the magnets were positioned in the upper slot region around the quadrature axis to reduce the quadrature axis flux. This rotor configuration is complicated and the presence of the flux barriers block the direct axis flux. CEM, a French company, developed a new type of brushless self starting synchronous motor known as Isosyn [5]. This motor led to the development of machines having higher efficiency, better power factor along with the elimination of rotor losses and reduced stator losses. Further development of rotor configurations [6-8], ensuring optimal use of expensive magnetic materials produced machines with high torque to inertia and high power to weight ratio.

A familiar rotor configuration of interior permanent magnet motor (IPM) which has been extensively researched [3-8] contains radially buried magnets inside the rotor core. Figure 1.1 shows one of these rotor configurations. Instead of circular flux barriers shown, radially oriented flux barriers can also be used. The motor of this rotor configuration is robust and suitable for high speed operation [9]. However this rotor configuration has a high quadrature axis inductance that is not desirable in vector control of PM motors [10].

The suitability of interior permanent magnet motors for field weakening applications was first investigated by Sneyers [11] and Jahns [12]. Sebastian and Slemon [13] examined the design of inset permanent magnet motors to optimize the field weakening performance, but Schiferl and Lipo [14] made the first serious attempt to determine the effect of varying the motor parameters on the field weakening performance. Further studies by Soong and Miller [15] examined the theoretical and practical limitations of field weakening performance of IPM motors. The applications of PM synchronous motors by means of flux weakening control led to the examination of the effects of the

magnetic saturation on the performance of motor [16]. Further studies are made on the flux-weakening scheme for an interior permanent magnet synchronous motor that enables the maximum torque operation for the fast acceleration in the constant power region according to the current and voltage limit condition [17-19].

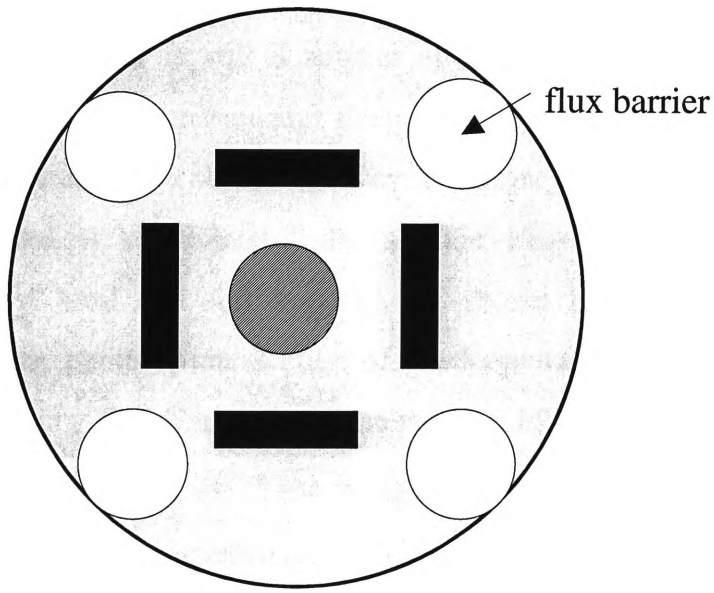

Figure 1.1 Radially oriented buried permanent magnet rotor configuration [9].

Further studies on permanent magnet motors involved are the harmonic fields and core losses, effects of saturation and effects of demagnetization and magnetization of magnets under different operating conditions [20-23]. Other aspects of PM motors which have been investigated in the recent years are the performance of the motor and the optimum design of the motor using computer simulation. Different techniques such as finite element methods, have been used for obtaining an optimum design and analyzing the performance of the machines [24-28].

1.3 Further details of permanent magnet machines

1.3.1 Permanent magnets

The development of permanent magnets with high energy density has led to increased interest in the use of permanent magnets for DC and AC synchronous machines. The representation of the magnetization characteristics of the magnets is difficult and is still a subject of research. However it is often acceptable to consider the permanent magnet to be ideal or linear [29-31]. A Soft magnetic material is characterized by a narrow hysteresis loop and hard magnetic material is characterized by a wide loop [32]. The hysteresis characteristics of hard and soft magnets are shown in Figures 1.2 and 1.3 respectively. The point of intersection of the loop with the ordinate is called residual flux density B_r. The point of intersection of the abscissa and the loop is called the coercive force, H_c. The straight line approximation of the second quadrant magnet (B-H) characteristics of a hard magnetic material is shown in Figure 1.4.

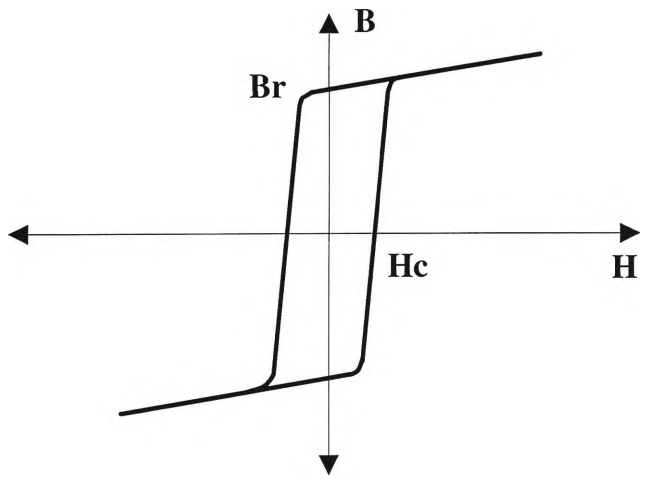

Figure 1.2 B-H relationship of a soft magnetic material

The B-H characteristics for some of the most used permanent magnet materials are shown in Figure 1.5 [33]. All of these PM materials have their magnetic domains well aligned resulting in an essentially straight line relationship in the

second quadrant of the B-H characteristics. However, if the flux density is reduced beyond the knee of the characteristic (denoted as flux density B_d as shown in Figure 1.5) some magnetism will be lost permanently.

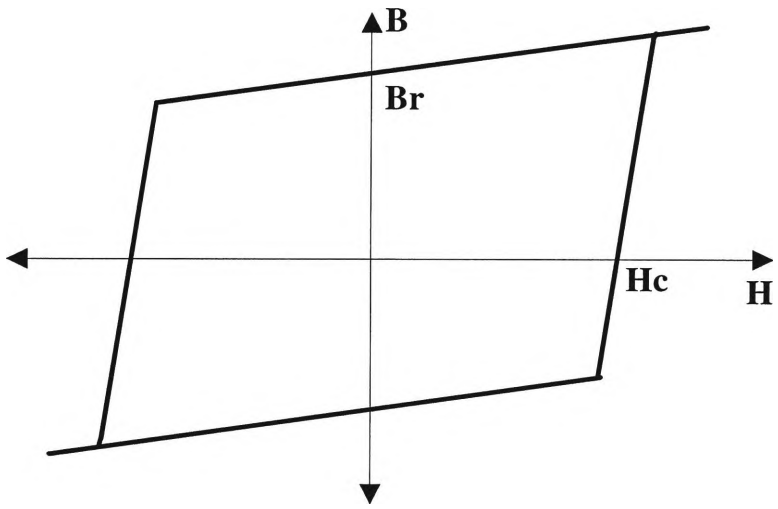

Figure 1.3 B-H relationship of a hard magnetic material

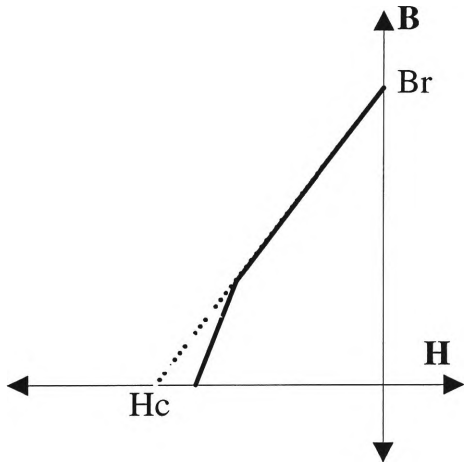

Figure 1.4 Straight line approximation of magnet characteristics

The cost of ferrite permanent magnet is attractively low but their residual flux density is only around 0.3-0.4T, which is much lower than the desired range of gap flux density in most machines. Samarium Cobalt magnets have a higher value of residual flux density (0.8-1.1T), but Neodymium Iron Boron (Nd-Fe-B)

has a residual flux density in the range of 1.1-1.4T, which is adequate to produce a flux density of 0.8-0.9T across a relatively large air gap with reduced magnet dimensions. The cost of Nd-Fe-B materials is still relatively high, largely because of the manufacturing complexity [33] and comparatively smaller demand.

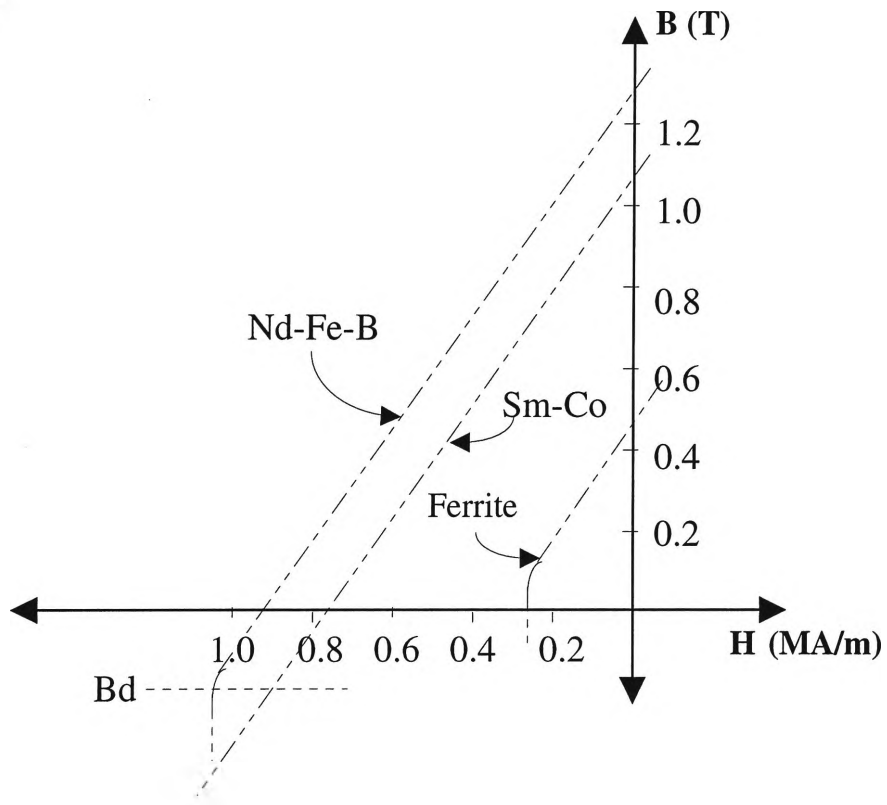

Figure 1.5 B-H characteristics for PM materials

1.3.2 Classification of permanent magnet motors

Permanent magnet (PM) motors can be classified into two types [33]. They are:

(i) Switched or trapezoidal permanent magnet motor and
(ii) Sinusoidal permanent magnet motor.

Switched or trapezoidal permanent magnet motors have stator windings that are supplied in sequence with near rectangular pulses of current. Hence the stator

windings are concentrated into narrow-phase belts. Sinusoidal machines are typically distributed over multiple slots in order to approximate a sinusoidal distribution. Hence trapezoidal excitation is preferred for PM machines with non salient rotor designs such as surface mounted permanent magnet motors in which the stator phase inductance remains constant as the rotor rotates. PM machines with salient rotor poles can offer better performance characteristics when excited sinusoidally thus providing flexibility for different rotor geometries which mainly includes inset or buried permanent magnet motors [13,34].

In a surface permanent magnet motor (SPM), the magnet bars are mounted on the rotor surface. Since the magnets have a very high reluctance, the machine can be considered to have a large effective air gap, which makes the effects of saliency negligible. In interior permanent magnet motors (IPM), the magnets are buried inside the rotor resulting in a mechanically robust construction.

The cross sections of the two types of rotors representing the quadrature axis (q-axis) and direct axis (d-axis) are shown in Figure 1.6 [35]. For SPM motors, the q-axis inductance and d-axis inductance are approximately equal but for IPM, the q-axis inductance is greater than the d-axis inductance.

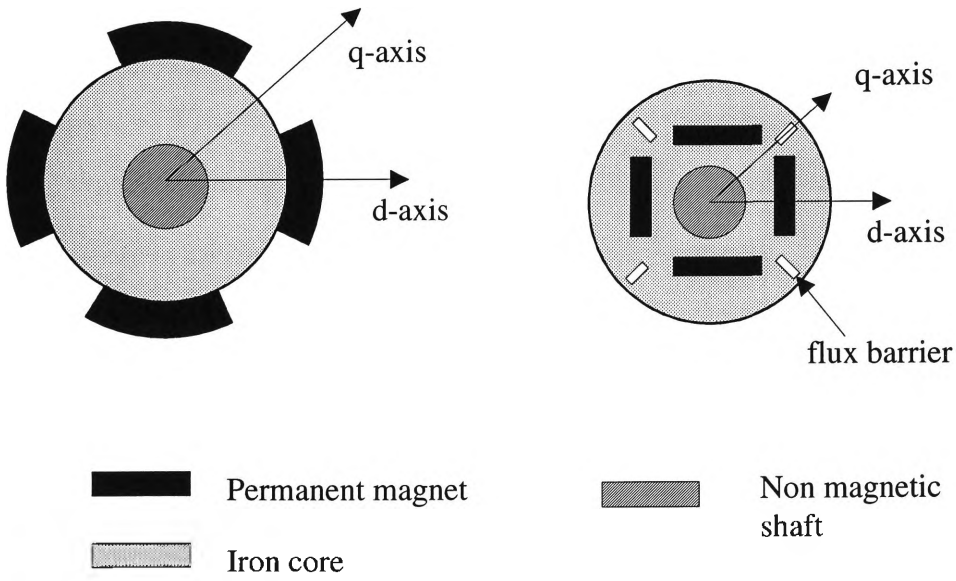

Figure 1.6 SPM and IPM motors

1.3.3 Comparison of permanent magnet motors

The comparison of IPM and SPM motors is based on some of the parameters such as torque, effective air gap, terminal voltage ratio, operating range of the magnets, demagnetizing coefficient and motor saliency. Terminal voltage ratio (TVR) [36] is defined as the ratio of on-load voltage to no-load voltage of the motor. Terminal Voltage Ratio thus determines the inverter capacity required to feed the motor. A comparison of the two types of permanent magnet motors is given in Table 1.1. Some of the factors such as torque, saliency characteristics, armature reaction and inverter voltage capacity of the IPM and SPM machines are compared.

It is seen from Equation (1.2) of Table 1.1, the net torque in the IPM motor arises from both the field alignment and reluctance action [37, 38]. The reluctance torque component is due to the interaction of the current induced magnetic flux linkages $L_d\, i_d$ and $L_q\, i_q$ with the orthogonal current components i_q and i_d respectively. The reluctance torque is related to rotor saliency, thus proportional to the axis inductance difference (L_d - L_q). The field alignment torque is due to magnet flux oriented in the rotor d-axis interacting with the q-axis stator current thus resulting in a torque proportional to product of magnetic flux linkage λ_m and q-axis stator current i_q. For an IPM motor, maximum torque can be obtained by using a torque angle greater than 90° as seen from the characteristics of Figure 1.7. To make use of the extra amount of the torque produced, the machine is usually operated at a torque angle greater than 90°. The two torque components are influenced by different factors such as saturation, harmonic fields and effective saliency of the rotor configuration. Hence the performance of the IPM machines can be improved by reducing the factors such as saturation, harmonic fields and effective saliency.

SPM	IPM
Torque expression is given by [30] $T_e = \frac{3P}{2}\left[\lambda_m i_q\right]$ (1.1) where, P is the number of poles, λ_m is the magnet flux linkage and i_q is the q-axis stator current. It can be seen from Equation (1.1) that the torque is proportional to current as in the case of a DC motor. Hence SPM machines are also known as brushless DC motors.	Torque expression is given by [30] $T_e = \frac{3P}{2}\left[\lambda_m i_q + i_d i_q \left(L_d - L_q\right)\right]$ (1.2) where, P is the number of poles, L_q is the q-axis stator inductance, L_d is the d-axis stator inductance, λ_m is the magnet flux linkage, i_q is the q-axis stator current and i_d is the d-axis stator current.
Has an effectively uniform airgap, thus exhibiting magnetically non-salient pole structure. In other words d-axis inductance L_d is equal to q-axis inductance L_q.	Exhibits saliency thus resulting in a difference in the values of d-axis inductance and q-axis inductance ($L_d \neq L_q$).
Because of the uniform and large air gap, the armature (rotor) reaction effects are negligible.	The armature reaction is large enough so that it cannot be neglected.
Since $\frac{L_d}{L_q}$ is equal to unity, the inverter voltage capacity required to feed the motor is less when compared to IPM motors.	High saliency ratio results in high terminal voltage ratio. Due to this the inverter voltage capacity required to feed the motor is relatively high.

Table 1.1 Comparison of PM motors

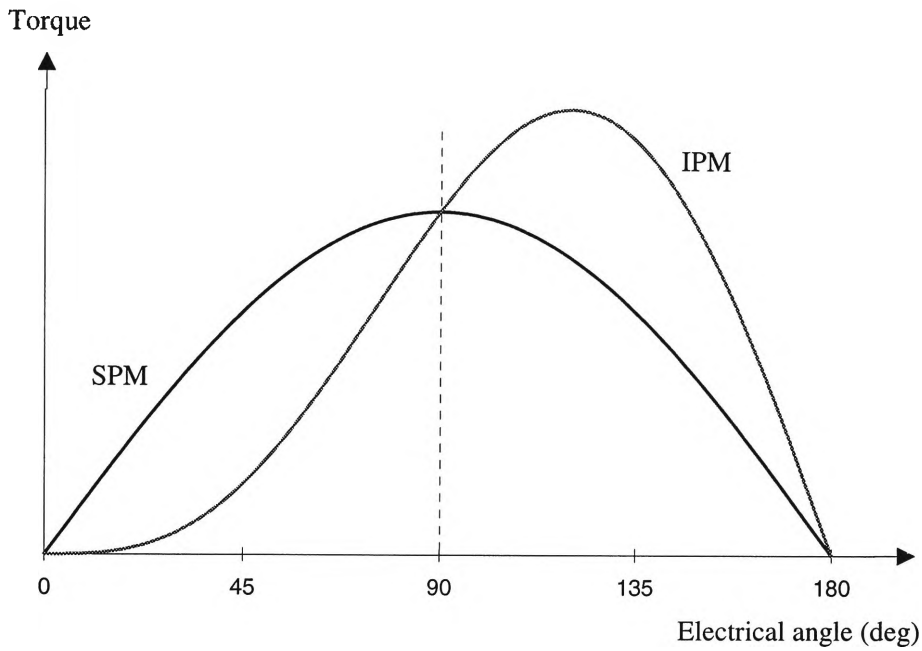

Figure 1.7 Torque-angle characteristics of SPM and IPM motors

1.3.4 Operating modes of permanent magnet motors

The torque-speed characteristics of a permanent magnet motor are divided into three modes of operation as shown in Figure 1.8 [15]. Mode 1 is the region from zero to rated speed (ω_r), where maximum torque can be obtained by operating at rated current. This region is commonly referred to as the current limited region. Mode 3 is the region where maximum torque is obtained with limited voltage. It is commonly referred to as the voltage limited region. Mode 3 region can be obtained by controlling the stator currents in such a way that the stator current space phasors contain a direct axis component along the negative direct axis of the rotor reference frame in addition to the quadrature axis stator current component. This region is also referred to as the field weakening region. Mode 2 is the region that lies between mode 1 and mode 3 and is commonly referred to as the current - voltage limited region.

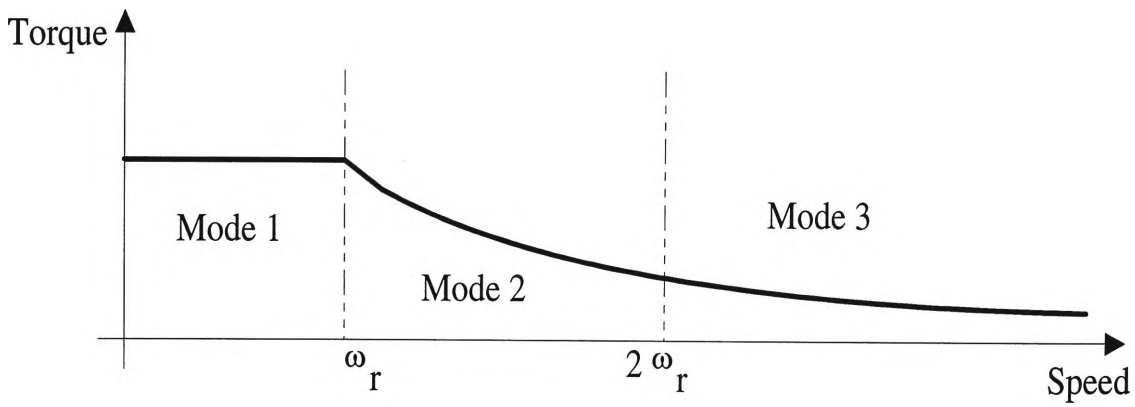

Figure 1.8 PM motor operating mode characteristics

1.3.5 Current control methods

Different control methods can be used on a motor in order to have different performance characteristics [39]. In permanent magnet (PM) motors, $i_d = 0$ control method, in which a direct axis component of stator current is absent, is applied in order to avoid demagnetization of permanent magnet. The development of PM materials, however, has brought materials with large coercive force. One such PM material, Nd-Fe-B has a high coercive force and requires a large negative i_d to demagnetize the magnets. Therefore, there is no longer a necessity to keep using conventional $i_d = 0$ control method and hence several control methods can be used to improve the ability of the PM motor system [39].

The direct axis flux path and the quadrature axis flux paths for an interior PM machine are shown in Figure 1.9. As seen from the figure the q-axis flux path passes through two air gaps but the d-axis flux path passes through four air gaps, that is, the magnet also acts like an air gap [10]. Higher value of air gap length along the d-axis results in a higher value of reluctance, resulting in a smaller value of d-axis inductance when compared with the q-axis inductance.

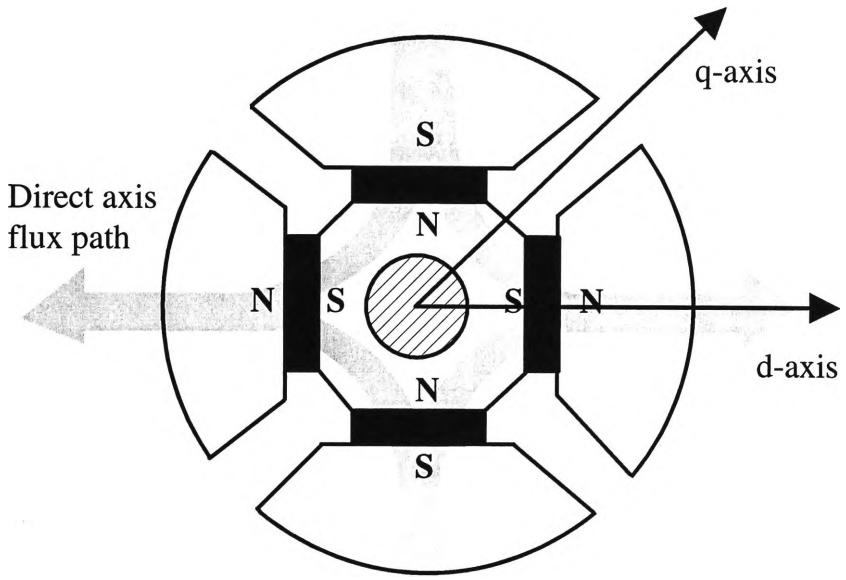

(a) d-axis flux path

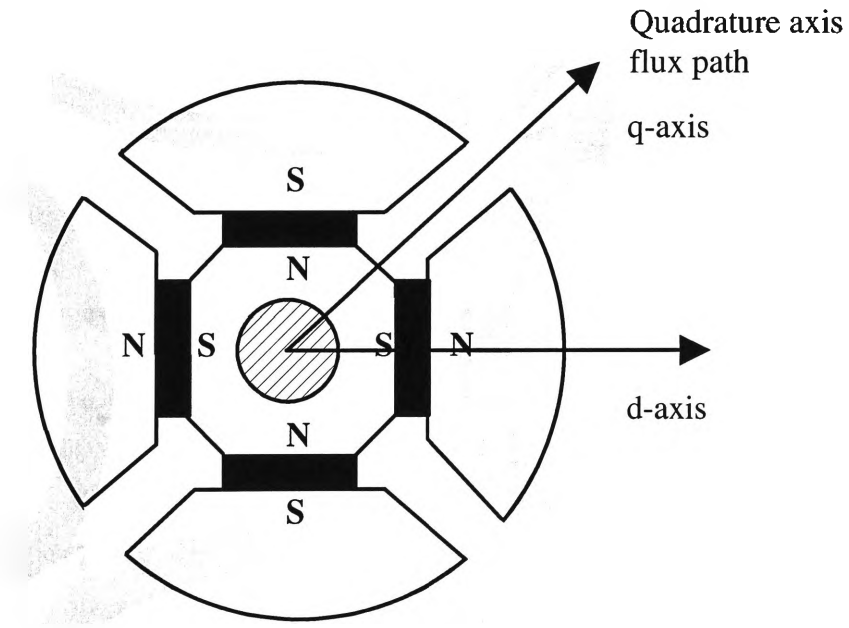

(b) q-axis flux path

Figure 1.9 Magnetic flux paths of IPM motors [10]

The torque equation of an interior permanent magnet motor shown previously by Equation (1.2) is $T_e = \frac{3P}{2}\left[\lambda_m i_q + i_d i_q \left(L_d - L_q\right)\right]$. If direct axis current i_d = 0, the torque just depends on the first term. But if i_d is made negative, the second term becomes positive thus resulting in an increase in torque, which is one of the requirements of the motor design. But care should be taken that the resultant per unit value of the current does not exceed very much from unity as the resultant current is equal to the vector sum of quadrature current i_q and direct current i_d [40-41]. The sinusoidal current excitation as illustrated in Figure 1.10 can also be expressed as an instantaneous current phasor i_s made up of d and q axis components i_d and i_q respectively [42].

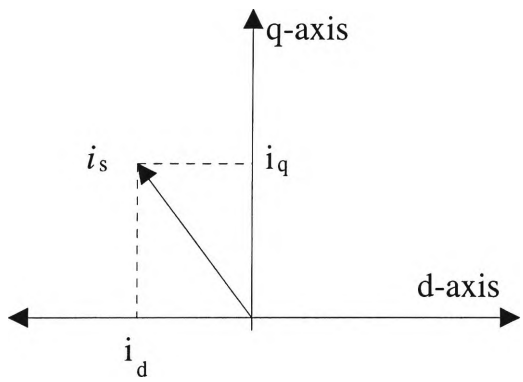

Figure 1.10 Current space phasors of PM synchronous motor

1.4 Temperature effects on permanent magnets

The use of neodymium-iron-boron (Nd-Fe-B) permanent magnet in electric motors is usually limited by their magnetic and thermal characteristics. This limitation mainly depends on the magnetic field intensity that can be applied to the magnets without demagnetization risks [43]. Permanent magnet (PM) motors using Nd-Fe-B can be operated at a temperature of about 140°C. In the normal range of operating temperature, the residual flux density and the intrinsic coercivity of the magnet will come down. This variation is a reversible process and hence when the temperature is reduced the flux density and coercivity will

revert to the original value. But when the operating temperature of the magnet is increased above a certain critical temperature, it will result in irreversible demagnetization of the magnet. The critical temperature at which the irreversible demagnetization occurs is a function of the magnet material and of the operating load line of the magnet. Hence to avoid demagnetization, the motor should be designed such that the normal operating temperature is below this critical temperature. As a result of the recent improvements in the PM materials, with the presently available Nd-Fe-B magnets, depending on the composition, PM motors can be designed for operation up to around 150°C [44].

1.5 Scope of the work and plan of the thesis

The work presented in this thesis is aimed at the design and optimization of an interior permanent magnet (IPM) synchronous motor. Rotor configuration of a PM motor is a major factor that influences its performance. Another important aspect that has to be considered in the motor design is the estimation of relevant motor design parameters. In this project, emphasis is placed on reducing the quadrature axis inductance, by means of which better vector control and faster dynamics of the machine is obtained. A general mathematical model of the IPM motor is developed and the optimum dimensions of the magnetic circuit of the rotor is determined. The optimization of the design is further refined by carrying out a sensitivity analysis on the parameters obtained. The results obtained from fine tuned optimized design of the IPM motor are further validated against the results from finite element analysis.

Chapter 2 Chapter 2 gives a detailed analysis of the basic concepts involved in the interior permanent magnet motor considered. A mathematical model of an IPM motor using a hypothetical stator winding distribution is developed in this chapter.

Chapter 3 In an IPM motor a relatively large quadrature axis inductance affects the capacity of the power electronics and response characteristics of the

motor drives. An expression for q-axis inductance and torque for both uniform and shaped air gap machines are derived in this chapter.

Chapter 4 The developed mathematical model of IPM machine can be verified using different computational techniques that are used to predict the performance of electrical machines. A general and more accurate method commonly used is the finite element method. This chapter presents an introduction to the particular finite element software used for the analysis and also explains the procedure adopted in determining the motor characteristics of the IPM motor described in this thesis.

Chapter 5 The comparison of inductance for a uniform and shaped air gap machines calculated from theoretical and finite element results are presented in this chapter. Results required for the design optimization of the selected IPM motor are also presented in this chapter.

Chapter 6 The design optimization of a 5.5 kW IPM motor is considered. This chapter provides the steps involved in the design and optimization of the particular frame size of the IPM machine considered for analysis. The results obtained are further verified using finite element analysis.

Chapter 7 Concluding remarks and future directions are given in this chapter.

CHAPTER 2

DEVELOPMENT OF THE MATHEMATICAL MODEL OF AN INTERIOR PERMANENT MAGNET MOTOR

2.1 Introduction

Rotor configuration of an interior permanent magnet (IPM) motor is a major factor that governs the performance of the motor. Air gap flux density is one of the very important aspects that influences the torque produced and other operating characteristics of the IPM motor. Different rotor configurations have different air gap flux density distributions and machine parameters. It has been previously shown that an increase in the air gap towards the rotor quadrature axis of an IPM motor will yield an improved torque and a reduction in the quadrature axis inductance [10]. The reduction in quadrature axis inductance makes the IPM machine suitable for better vector control operation giving faster dynamic characteristics for the machine. Also with a lower quadrature axis inductance, the constant torque regime can be extended for a given inverter bus voltage. Another important aspect that has to be considered in the motor design is the theoretical estimation of relevant motor design parameters. The ability to optimally select the design parameters of a particular machine to meet the given operating requirements and constraints are also of significant importance in the motor design. Hence for design optimization, design sensitivity expressed in terms of design variables is required. The design sensitivity analysis is carried out to evaluate the variation of an objective function with respect to changes of design variables. Hence it is desired to develop a sensitivity expression in terms of design variable variations. The combination of sensitivity analysis with optimization techniques leads to optimum design parameters. In this chapter, basic concepts of IPM motors involving torque equation, calculation of magnetic flux density and effects of air gap profile are presented. An expression for the

shaped air gap profile is also derived. A mathematical model required for the design optimization of an IPM motor is also presented in this chapter.

2.2 Concepts of interior permanent magnet motor

2.2.1 Torque equation

The torque equation of an IPM motor as expressed in Equation (1.2) in Table 1.1 of Chapter 1 is given by:

$$T_e = \frac{3P}{2}\left[\lambda_m i_q + i_d i_q \left(L_d - L_q\right)\right] \tag{2.1}$$

As discussed in Chapter 1, the torque of an IPM machine depends on both the field alignment torque and the reluctance torque. The reluctance torque that is related to rotor saliency is proportional to the axis inductance difference $\left(L_d - L_q\right)$.

2.2.2 Cogging torque

In synchronous machines with interior permanent magnets (PM), one of the requirements of the motor design is the smooth torque operation. In a PM machine, this smooth torque operation is prevented due to the presence of cogging torque that arises from the interaction of rotor magnets with teeth on the stator [54]. Hence cogging torque must be reduced. The reduction of cogging torque can be achieved in a number of ways such as, shaping of the magnets, skewing of the stator, coordinating the design of the number of the slots, slot opening and magnet dimensions. However the skewed rotor construction is costly in the case of permanent magnets, because it is difficult to manufacture the magnets in complex geometric shapes. Furthermore, the required magnetizing techniques can result in lower flux levels [41].

2.2.3 Effect of the air gap profile

Air gap length is an important factor that influences the torque production in an IPM motor. Permanent magnets having permeability almost equal to that of air, acts like an air gap along the rotor d-axis in an IPM machine. Hence changes in the air gap length along the rotor d-axis will not have a significant effect on the d-axis inductance in an IPM machine. Conversely, even a small change in the air gap length along the rotor q-axis, will have a significant effect on the q-axis inductance. Any increase in the air gap length leads to a reduction in the q-axis inductance.

It can be seen from the torque Equation (2.1), motor saliency is one of the factors that affect the torque capability of the IPM machine. Also the motors are current controlled and the inverter capacity required to feed the motor is determined by the terminal voltage ratio, which further depends on the saliency ratio. Hence for faster current control of the motor, the saliency ratio has to be small. In other words the q-axis inductance (L_q) has to be small. One way of reducing the q-axis inductance of the motor is by increasing the air gap length towards q-axis of the motor. The increase in air gap length also increases the reluctance of the stator flux paths and restricts the flux which in turn, reduces the air gap flux density wave distortion resulting in a reduction in harmonics. Further as discussed previously, the cogging torque arises primarily due to the sharp change of the airgap flux density under the teeth at the edges of the poles of the rotor as the rotor is moved. In the case of the machine with increased airgap towards the q-axis, the airgap flux density under the tooth experiences a smooth variation towards the edges of the poles thus reducing the cogging torque significantly [10].

2.2.4 Uniform and Shaped airgap machines

The rotor structure of the interior permanent magnet (IPM) machine considered in this thesis is similar to the IPM rotor configuration shown in Figure 1.6 of

Chapter 1. The interpolar regions of the rotor are eliminated in order to reduce the leakage fluxes from pole to pole. This machine is referred to as the uniform airgap machine. Figure 2.1 shows the rotor configuration of the uniform airgap machine. The uniform airgap machine consists of a stator similar to that of a conventional induction motor and the rotor with interior permanent magnets. The rotor is fitted with four separate poles each of which consists of a Neodymium-Iron-Boron (Nd-Fe-B) permanent magnet bolted on to the rotor core on the shaft.

The airgap length along the q-axis of the motor is increased by shaping the airgap profile of the uniform airgap machine. Figure 2.2 shows the rotor configuration of the shaped airgap machine. The shaped airgap machine consists of a stator similar to that of a uniform airgap machine except that the rotor is shaped to obtain an increasing airgap length towards the interpolar region.

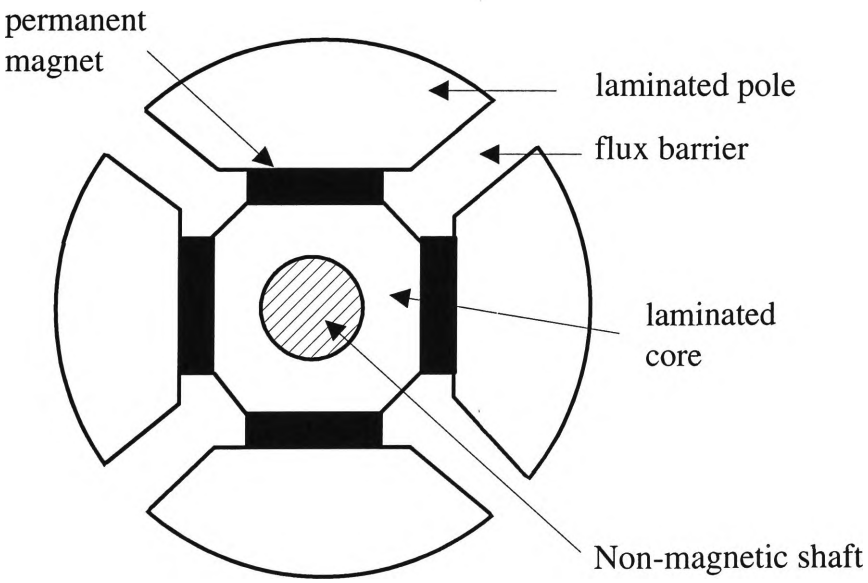

Figure 2.1 Rotor configuration of the uniform airgap machine

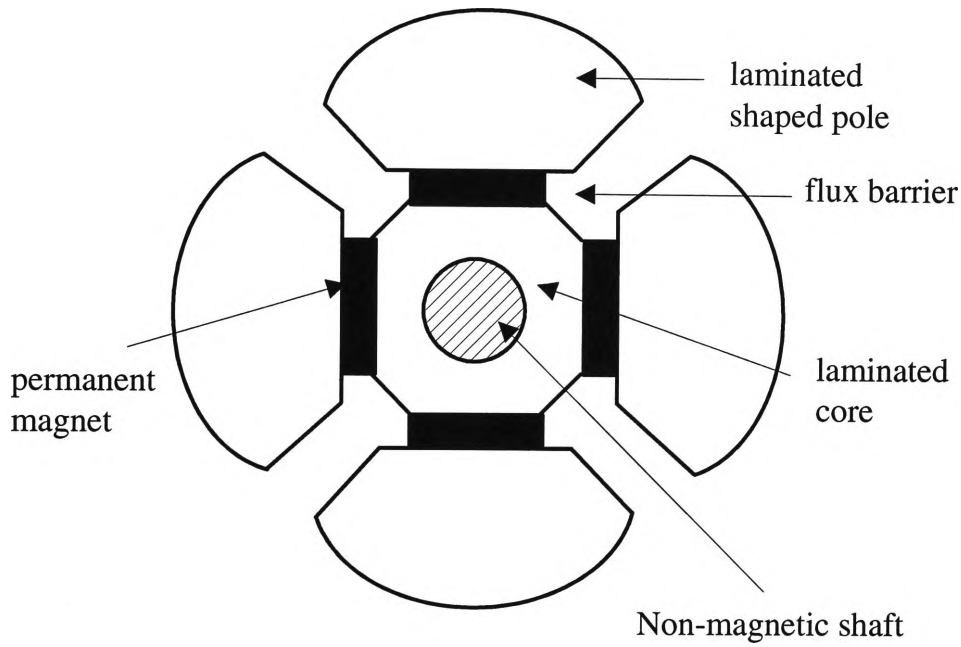

Figure 2.2 Rotor configuration of the shaped airgap machine

2.2.5 Development of the rotor airgap profile

A 4-pole interior magnet rotor configuration having a smooth, uniform airgap is considered in the development of the airgap profile. A simplified magnetic circuit of the chosen uniform airgap machine ignoring the stator slots and representing a ¼ model of the 4 pole machine is shown in Figure 2.3. For the continuous flux path corresponding to angle θ due to the magnets shown in Figure 2.3, the MMF balance, as a function of airgap length, flux density in the magnet and airgap, coercivity and thickness of the magnet, can be written as shown:

$$2 H_c g_m = 2 H_m g_m + 2 H_a g_a + F_{mi} \tag{2.2}$$

where,

H_c = coercivity of magnet,

g_m = thickness of the magnet,

g_a = airgap length,

H_m = magnetic field intensity in magnet,

H_a = magnetic field intensity in airgap, and

F_{mi} = MMF drop in stator and rotor steel.

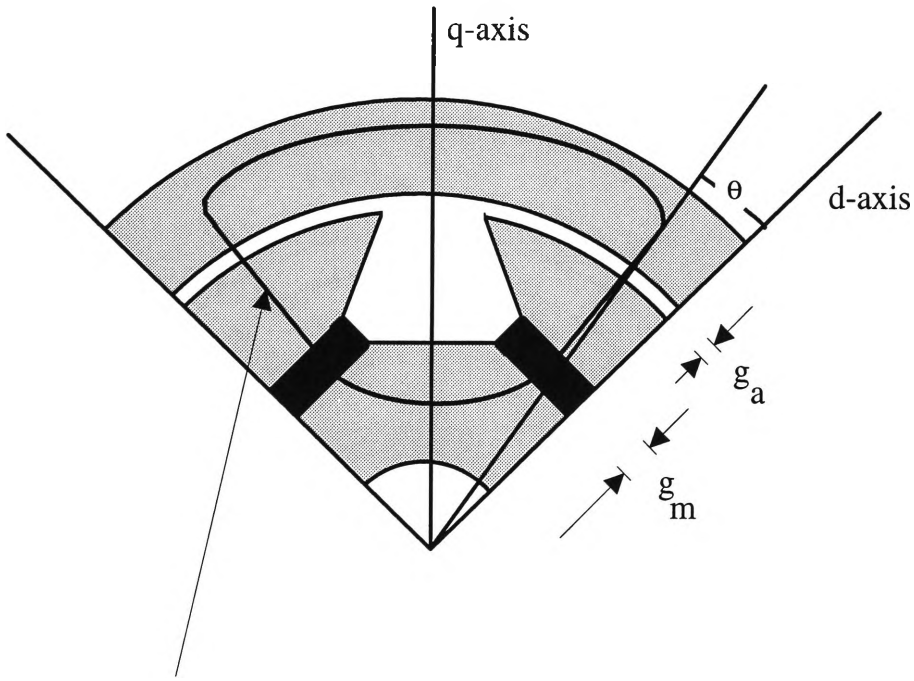

g_m = thickness of the magnet

g_a = airgap length

Figure 2.3 A continuous flux path of field due to the magnets

The relative permeability of the space occupied by the magnets can be assumed to be equal to that of air as the magnet material used is Nd-Fe-B. Further, the MMF drops in the stator and rotor steel are ignored. Therefore, Equation (2.2) can be rewritten as:

$$B_a\, g_a = (B_r - B_m)\, g_m \tag{2.3}$$

where B_a = flux density in airgap,

B_r = remanent flux density of magnet and

B_m = operating flux density of the magnet.

The operating flux density of the magnet B_m can be expressed as a function of maximum (peak) airgap flux density (B_p), radius of the rotor (r) and the width of the magnet (W). The expression for B_m is derived employing Figure 2.4.

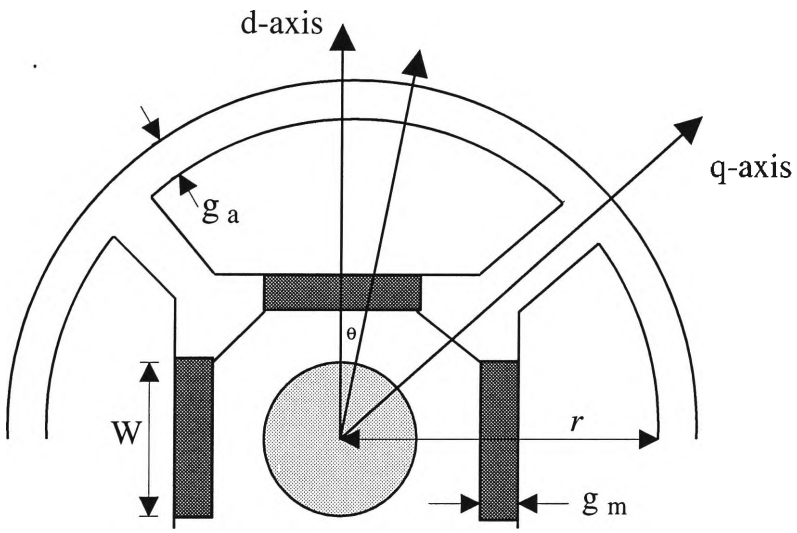

Non magnetic shaft

Permanent magnet (Nd-Fe-B)

r = radius of the rotor

W = width of the magnet

g_m = thickness of the magnet

g_a = length of the airgap

θ = electrical angle

Figure 2.4 Cross section of interior permanent magnet motor

Ignoring the MMF drops in steel, Equation (2.2) can be written as:

$$2 H_c g_m = 2 H_m g_m + 2 H_a g_a$$

For a uniform airgap machine, the airgap flux density B_a will be the same for all values of θ, where θ is the electrical angle measured from the rotor direct axis. In the shaped airgap machine, the required airgap flux density is of a sinusoidal form and is given by $B_p \sin\theta$, where B_p is the maximum (peak) airgap flux density. From Figure 2.4, the value of flux ϕ at the particular angle θ is given by the product of the airgap flux density at the angle θ and the area, which is given by the product of the length of the machine ℓ and the radius of the rotor r. Hence the total flux per pole at the airgap can be calculated by integrating the flux obtained at each angle θ extending from 0° to 90°.

$$\text{Flux per pole at the airgap} = 2 \int_0^{\frac{\pi}{2}} B_p \sin\theta \; \ell \; r \; d\theta = 2 B_p \; \ell \; r \tag{2.4}$$

The total flux passing through the magnet can be given by:

$$\text{Flux passing through the magnet} = B_m \; W \; \ell \tag{2.5}$$

The net magnetic flux entering and leaving the closed surface, ignoring any pole to pole flux leakage, is equal to zero. Hence Equations (2.4) and (2.5) can be equated giving an expression shown below:

$$B_m = \frac{2 B_p \; r}{W} \tag{2.6}$$

The expression in Equation (2.6) is derived based on the assumption that the magnetic flux density within the magnet is uniformly distributed inside the magnet. Previous finite element studies [10] have also found the magnetic flux density of the magnet to be uniform except for small variations.

The structure of the shaped airgap machine is shown in Figure 2.5. The minimum airgap length g_{min} of the shaped pole machine is made equal to the airgap length of the uniform airgap machine. This is an arbitrary decision made,

which is useful when comparing the uniform and shaped airgap machines. Except for the differences in the airgap profile, all other machine dimensions of the shaped airgap machine are maintained the same as that of the uniform airgap machine. As seen from the Figure 2.5, the shaping of the airgap profile is such that the airgap length at the edge of the pole is g_{max}.

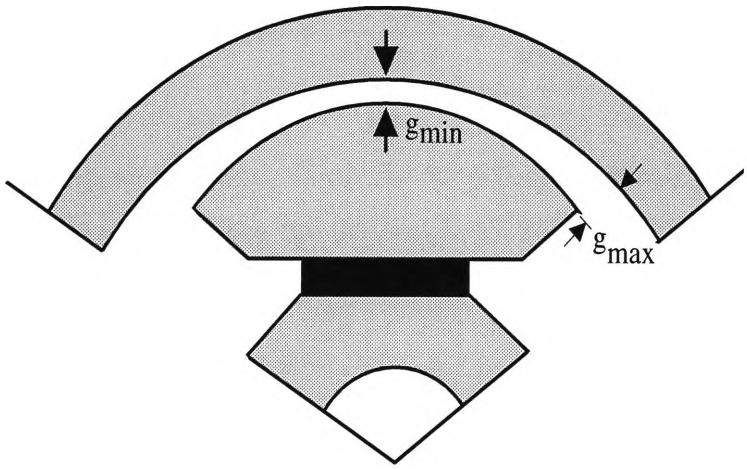

g_{max} = Maximum air gap length

g_{min} = Minimum air gap length

Figure 2.5 Shaped airgap profile

The MMF balance for a shaped airgap machine as shown for uniform airgap machine in Equation (2.3) is :

$$B_a(\theta)\ g_a(\theta) = \left(B_r - B_m\right) g_m$$

where $B_a(\theta)$ is the airgap flux density of the shaped airgap machine given by $B_p \sin\theta$ and $g_a(\theta)$ is the shaped airgap length at angle θ. The value of $g_a(\theta)$ at the end of the pole angle, as shown in Figure 2.5, is equal to g_{max}.

Hence the expression for the product of $B_a(\theta)$ and $g_a(\theta)$ can be given by:

$$B_a(\theta)\, g_a(\theta)\Big|_{\theta=\theta_{re}} = B_p\, g_{max}$$

The expression obtained can be generalized for all angles of θ as shown:

$$g_a(\theta) = \frac{B_p\, g_{max}}{B_p\, sin\, \theta} = \frac{g_{max}}{sin\, \theta} \tag{2.7}$$

For the shaped airgap machine, along the rotor d-axis ($\theta = 0$), the length of the airgap is equal to g_{min}. Hence the expression in Equation (2.7) can be rewritten as:

$$g_\theta = \frac{g_{min}}{cos\, \theta} \tag{2.8}$$

The range of electrical angle θ in Equation (2.8) extends from 0° to an angle less than 90°, because of the presence of the interpolar region. The derived expression can be verified for a prototype machine by calculating the values of the airgap length for different angles of θ as shown in Table A1 of Appendix A.

2.3 Mathematical model of interior permanent magnet motor

2.3.1 Need for a mathematical model

The ability to optimally select the design parameters of a particular machine to meet the given operating requirements and constraints is of significant importance in the motor design. Shape optimization of the permanent magnet is one of the major criteria in the design of the interior permanent magnet motor. Depending on the shape of the permanent magnet, equal volumes of magnetic material produce different amounts of flux. In a general design approach, a permanent magnet is designed to obtain specified flux levels in the airgap and

the shape of the magnet is designed to reduce the volume [25].

The design of a permanent magnet is further complicated by the fact that the reluctance of a permanent magnet increases with its volume and the volume of the permanent magnet in a magnetic circuit is directly proportional to the leakage factor [24, 45]. Thus it can be clearly seen that conventional techniques for design optimization of PM machines are inefficient and usually gives near optimal designs. A mathematical model expressing the optimum design from the best acceptable designs would provide a more accurate optimization technique. Therefore for a more accurate and cost effective design, a mathematical model expressing the optimum design parameters is required. The design optimization of the IPM machines presented in this thesis makes use of a mathematical model expressing the design parameters particularly the quadrature axis inductance.

2.3.2 Assumptions

The practical IPM motor having a discrete stator winding distribution cannot be easily generalized as it consists of a particular stator winding configuration. In order to have a general mathematical model of an IPM motor, an IPM machine with a hypothetical stator winding distribution is considered. In a practical machine with a uniform air gap, the sinusoidal distribution of MMF is usually achieved by distributing the winding into different slots having coils with equal number of turns. In the machine with hypothetical winding distribution the required sinusoidal distribution of MMF is achieved by distributing the coils on an incremental basis around the periphery. The effect of stator slots on airgap in the IPM machine considered are neglected thus removing the necessity for the use of Carter's coefficient in the expression for inductance. The MMF drop in the iron core are also neglected.

2.3.3 Calculation of the peak number of turns

The machine with hypothetical stator winding distribution needs to produce a peak air gap flux density equal to that of a practical machine having discrete stator winding distribution. This has to be achieved by finding a suitable value for the peak number of turns (N_p) in the machine with hypothetical stator winding distribution. The calculation of peak number of turns can be carried out by comparing the air gap flux density obtained in the practical machine as well as the machine with hypothetical winding distribution.

For a practical machine having a distributed winding, the peak value of fundamental MMF is given by:

$$\frac{4}{\pi} \frac{N_{ph}}{P} I K_w$$

where P is the number of poles, I is the rated current, N_{ph} is the number of turns per phase and K_w is the winding factor. Thus the maximum (peak) air gap flux density B_p is given by:

$$B_p = \mu_0 \frac{4}{\pi} \frac{N_{ph}}{P} I K_w \frac{1}{g} \tag{2.9}$$

where μ_0 is the permeability of free space and g is the length of the airgap.

Let the stator winding distribution in the hypothetical machine be given by the expression:

$$N(\theta) = N_p \cos \theta \tag{2.10}$$

where N_p is the peak number of turns and $N(\theta)$ is the number of turns in a coil at a position θ. For a peak current I the air gap MMF distribution due to a coil

positioned at an electrical angle θ is shown in Figure 2.6.

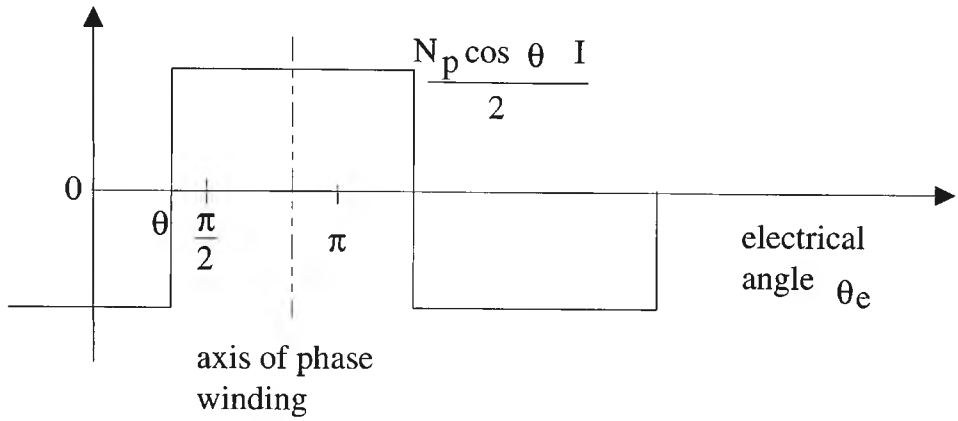

Figure 2.6 MMF distribution due to a coil at angle θ

The total MMF at an angle θ due to total number of turns present in the coil is given by:

$$I \int_{0}^{\theta} \frac{N_p}{2} \cos\theta \, d\theta \; - \; I \int_{\theta}^{p\pi} \frac{N_p}{2} \cos\theta \, d\theta$$

which can be simplified to $I N_p \sin\theta$. Therefore the air gap flux density at θ can be given by the expression:

$$B(\theta) = \frac{\mu_0 \, mmf(\theta)}{g} = \mu_0 \frac{N_p I}{g} \sin\theta = B_p \sin\theta \qquad (2.11)$$

The peak number of turns can be calculated by equating Equation (2.9) and Equation (2.11) respectively, i.e.:

$$B_p \text{ (practical)} = B_p \text{ (hypothetical)}$$

Hence the peak number of turns N_p in the machine with hypothetical stator winding is given by:

$$N_p = \frac{4}{\pi} \frac{N_{ph}}{P} K_w \qquad (2.12)$$

2.4 Summary

A discussion of the basic concepts involved in the interior permanent magnet motor was given in this chapter. This chapter also developed a mathematical model for the IPM motor having a hypothetical stator winding distribution. The calculation of peak number of turns in the hypothetical machine required to produce a maximum (peak) air gap flux density equal to that of the practical machine was also carried out.

CHAPTER 3

DERIVATION OF EXPRESSIONS FOR Q-AXIS INDUCTANCE AND TORQUE

3.1 Introduction

The inductance of the IPM machine influences the behavior of power electronic system driving the machine. Any variations in the airgap length, especially along the rotor q-axis results in a significant variation in the q-axis inductance. Hence inductance is one of the principal parameters that assist the design and development of the mathematical model of the IPM motor. The airgap flux density wave is also related to the instantaneous torque, the average and pulsating torques developed by the permanent magnet machines [46]. This chapter gives a detailed calculation of the q-axis inductance and the expression for torque for a uniform airgap machine and shaped airgap machine.

3.2 Calculation of inductance for uniform air gap machine

A general representation of a uniform airgap machine including its stator winding distribution is shown in Figure 3.1. This machine consists of a hypothetical stator winding distribution with the peak number of turns (N_p) along the rotor direct axis. Hence the air gap flux density produced will be sinusoidal and is maximum along the rotor quadrature axis. As discussed in Chapter 2, the winding distribution is given by the expression $N(\theta) = N_p \cos\theta$ where θ is the angle measured from rotor d-axis. Although for simplicity, the mathematical model considered is related to a 2 pole machine, the results presented are adjusted by the corresponding pole pair number depending on the number of poles present in the actual machine.

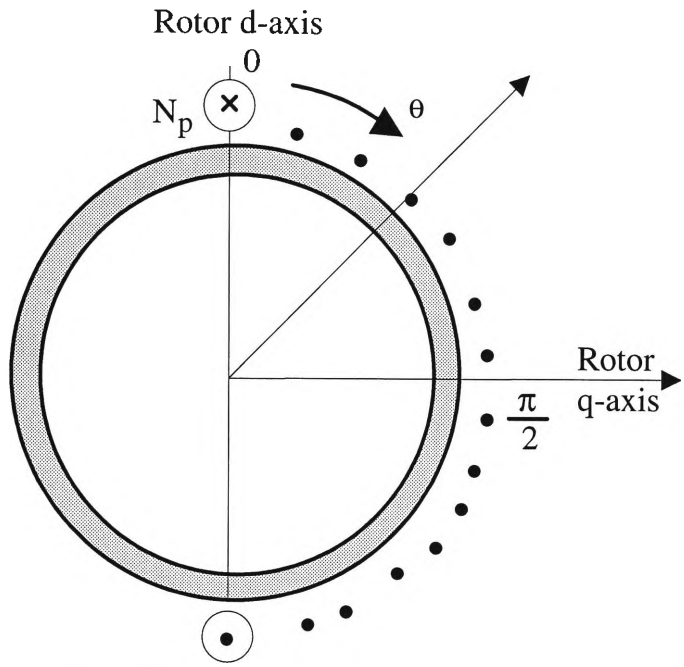

N_p = peak number of turns

θ = Electrical angle measured from rotor d-axis

Figure 3.1 General representation of a uniform airgap machine

In an interior permanent magnet machine the magnets will lead to leakage fluxes between poles along with the useful flux that crosses the airgap. In order to reduce the pole to pole leakage flux, the pole arc angle is made less than 180° electrical providing an interpolar region. It is also required to find an optimum value of the pole arc angle to avoid concentration of flux in a small area that results in saturation. The pole arc angle is equal to $\pi - 2\alpha = 2\theta_{re}$, as shown in Figure 3.2. Or in other words, the rotor iron in the interpolar region are eliminated.

The primary step that is carried out using the mathematical model is the selection of the flux tube at a position θ subtending an angle $d\theta$ as shown in Figure 3.2. For the 2 pole machine considered the incremental flux ϕ passing through the flux tube is given by the product of the flux density at the particular angle θ and the cross sectional area of the flux tube as shown in Equation (3.1).

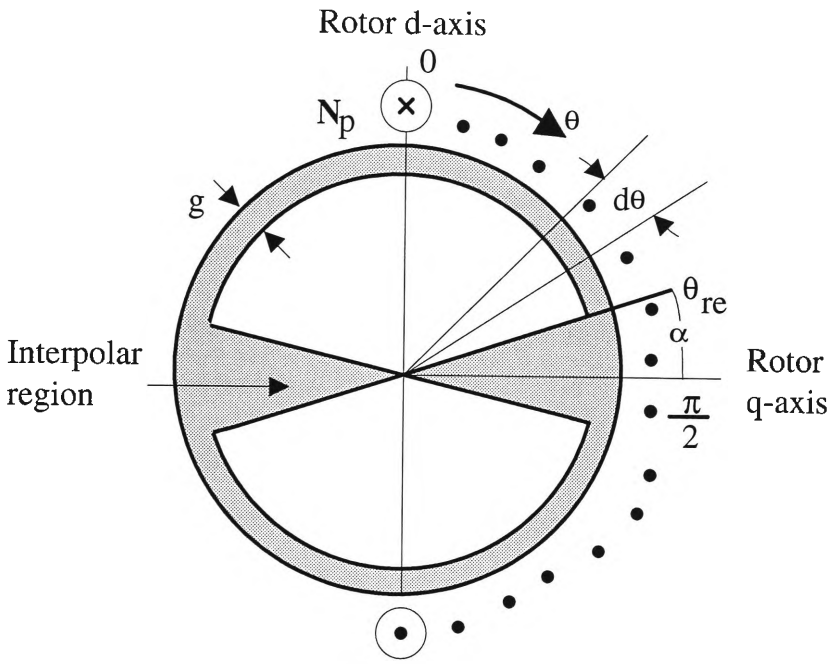

Figure 3.2 Representation of a uniform air gap machine with reduced pole arc angle

$$\phi = B_p \sin\theta \; r\ell \; d\theta \tag{3.1}$$

For a P-pole machine, the above expression is given by:

$$\phi = B_p \sin\theta \; r\ell \frac{2}{P} d\theta \tag{3.2}$$

In Equation (3.2), r is the radius of the rotor, and ℓ is the length of the machine. The total number of turns (N_t) linking the flux tube at the position θ can be calculated by finding the resultant sum of the number of turns from the rotor d-axis to the angle θ. This is obtained by integrating the total number of turns between the limits 0 to the angle θ and multiplying the resultant by a factor 2 to consider the effective number of turns in a single pole, as shown in Equation (3.3).

$$N_t = 2 \int_0^{\theta} N_p \cos\theta \, d\theta = 2 N_p \sin\theta \tag{3.3}$$

The flux linkage is given by the product of total number of turns linking the flux. The useful flux that crosses the airgap covers an angle between $-\theta_{re}$ to θ_{re}. Hence for a P pole machine the total flux linkage (φ_t) can be calculated as:

$$\varphi_t = P \int_0^{\theta_{re}} 2 N_p \sin\theta \; B_p \sin\theta \, r \ell \, \frac{2}{P} \, d\theta \tag{3.4}$$

The quadrature axis inductance L_q is equal to the ratio of flux linkage and the current. The value of B_p in flux linkage expression of Equation (3.4), can be obtained from Equation (2.11) of Chapter 2. Thus the quadrature axis inductance for a uniform airgap machine as a function of θ_{re} is given by:

$$L_q = \frac{\varphi_t}{I} = (N_p)^2 \mu_0 \, r \ell \, \frac{1}{g} \left(2\theta_{re} - \sin 2\theta_{re} \right) \tag{3.5}$$

3.3 Calculation of inductance for shaped airgap machine

The general representation of a shaped air gap machine with a reduced pole arc angle indicating its stator winding distribution is shown in Figure 3.3. The air gap profile as shown in the Figure 3.3, is minimum along the rotor direct axis and maximum at the pole edges closer to the quadrature axis. The shaping of the airgap profile is given by the expression of Equation (2.8) of Chapter 2.

$$g_\theta = \frac{g_{min}}{\cos\theta} \tag{3.6}$$

where g_{min} is the minimum airgap length of the machine.

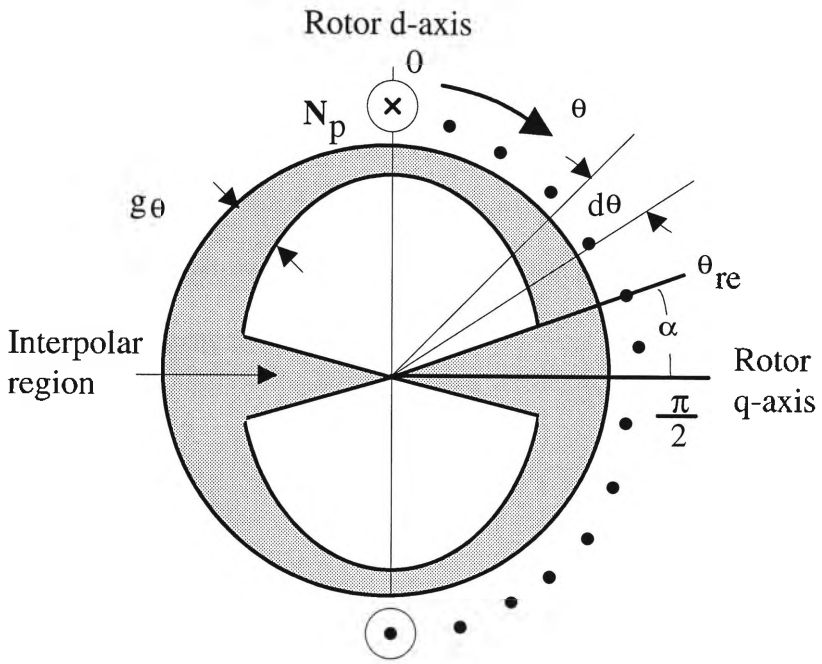

Figure 3.3 Representation of a shaped airgap machine with reduced pole arc angle

The procedure used for the derivation for the q-axis inductance for a uniform airgap machine is also followed for the shaped airgap machine. As before the incremental flux for a P pole machine, passing through the flux tube $d\theta$ shown in Figure 3.3 is given by:

$$\phi = \mu_0 \frac{N_p I}{g_\theta} \sin\theta \; r\ell \frac{2}{P} d\theta \tag{3.7}$$

where g_θ is the airgap profile of the shaped airgap machine depending on the angle θ. The expression for the total number of turns (N_t) linking the flux tube at an angle θ is same as that given by Equation (3.3) for the uniform airgap machine.

$$N_t = 2 N_p \sin\theta \tag{3.8}$$

Hence the total flux linkage, using the Equations (3.6 - 3.8), can be calculated by integrating the product of total number of turns linking the flux between the limits 0° to θ_{re} and multiplying by the factor P for a P-pole machine. The total flux linkage for the machine is:

$$\varphi_t = P \int_0^{\theta_{re}} 2 N_p \sin\theta \; \mu_0 \frac{N_p I}{g_\theta} \sin\theta \; r \ell \; \frac{2}{P} d\theta \tag{3.9}$$

Hence the expression of the quadrature axis inductance L_q for the shaped airgap machine as a function of the reduced pole arc angle θ_{re}, which is equal to the ratio of flux linkage and the current is given by:

$$L_q = (N_p)^2 \mu_0 r \ell \frac{1}{g_{min}} \frac{1}{3} \left(3 \sin\theta_{re} - \sin 3\theta_{re} \right) \tag{3.10}$$

3.4 Calculation of torque

3.4.1 Uniform airgap machine

In a uniform air gap machine the air gap length is constant irrespective of the position of rotor axis. The air gap flux density distribution due to the magnets in a uniform air gap machine is shown in Figure 3.4. From Figure 3.4, the flux density due to the magnets is given by Equation (3.11).

$$\begin{aligned} B(\theta) &= B_p \qquad 0 < \theta < \frac{\pi}{2} \\ B(\theta) &= -B_p \qquad \frac{\pi}{2} < \theta < \pi \end{aligned} \tag{3.11}$$

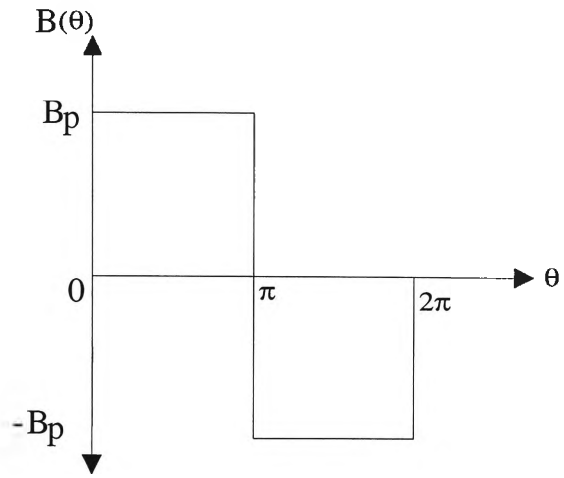

Figure 3.4 Flux density distribution due to the magnets in a uniform air gap machine

When a current lies in a magnetic field over an active length, a mechanical force is developed which is given by product of magnetic field intensity, current and the active length. For the uniform air gap machine with hypothetical stator winding distribution, the force F can be written as:

$$F = B_p I N_p \cos(\theta + \delta)\, \ell \tag{3.12}$$

where δ is the load angle. The incremental torque (T) produced on a conductor at an angle θ for a rotor radius r is given by:

$$T = B_p I N_p \cos(\theta + \delta)\, r \ell \tag{3.13}$$

Thus the total torque T_t produced by the machine can be calculated by adding the incremental torques for all the positions of θ extending from 0° to 180°. This is obtained by integrating the incremental torque from Equation (3.13) using the limits 0 to π and multiplying by the factor P for a P pole machine. The expression for the torque produced in a uniform airgap machine is shown in Equation (3.14).

$$T_t = P \int_0^{\pi} T \, d\theta = 2 P B_p I N_p \ell r \sin \delta \qquad (3.14)$$

3.4.2 Shaped air gap machine

In a shaped air gap machine the air gap flux density due to the magnets is given by the expression $B_p \cos \theta$. The rectangular flux distribution produced by the magnets in a uniform airgap machine has a fundamental component equal to 4/π times the peak flat topped value of Figure 3.4. Hence the air gap flux density distribution due to the magnets in a shaped pole machine is sinusoidal in shape having a peak value at 4/π B_p as shown in Figure 3.5.

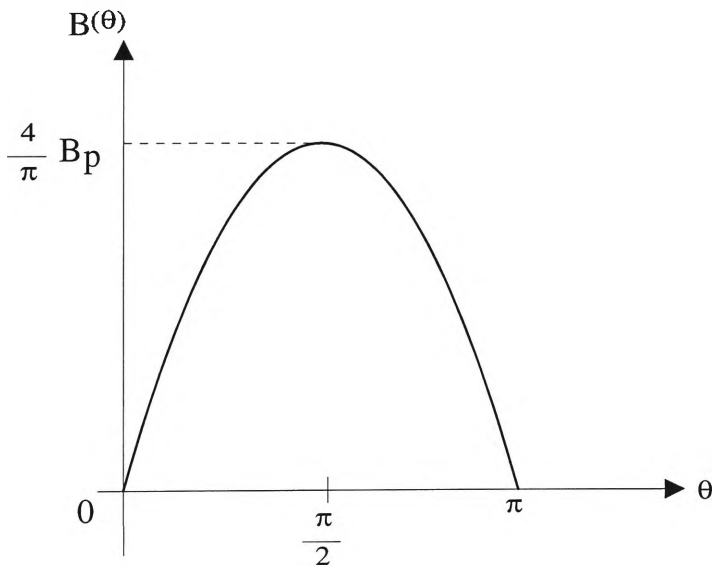

Figure 3.5. Flux density distribution due to the magnets in a shaped air gap machine

Similar to the uniform air gap machine the total torque for the shaped air gap machine can also be calculated as:

$$T_t = P \int_0^{\pi} \frac{4}{\pi} B_p \cos \theta \; I \; N_p \; \ell r \cos(\theta + \delta) \, d\theta$$

$$= 2PB_p IN_p \ell r \sin\delta \tag{3.15}$$

It can be seen from the torque expressions given by Equations (3.14) and (3.15) that there is no difference in magnitude between the torque developed by the shaped pole machine and the uniform air gap machines. Although both uniform and shaped air gap machines produce torques of similar magnitude, a small difference in torque levels at higher values of current exists because of the saturation effects along the quadrature axis in the uniform airgap machine. Due to the shaping of the air gap profile, the shaped pole machine is affected less by magnetic saturation than the uniform air gap machine and hence is capable of producing a slightly higher torque [10].

3.5 Summary

The calculation of inductance and torque that has been carried out using a mathematical model for an interior permanent magnet (IPM) motor was presented in this chapter. Inductance expressions for both uniform and shaped airgap machine were also derived in this chapter. The shaping of the airgap profile that influences the quadrature axis inductance was also discussed.

CHAPTER 4

FINITE ELEMENT ANALYSIS

4.1 Introduction

There are a variety of methods involved in the analysis of electrical machines. Development of equivalent circuits using experimental data to meet the requirements is one of the most commonly used analysis techniques. But the models of the electromagnetic machines in the form of equivalent circuits always need assumptions and approximations that limit the validity of such circuits. Moreover, especially for an interior permanent magnet machine (IPM), the design parameters of the equivalent circuit are variable with operating conditions [47]. Hence the analysis of performance under different operating conditions is very tedious. A popular and more accurate computational technique used to predict the performance of the electric machines is the finite element method [48]. Unlike in other computational techniques, some of the features like saturation of magnetic materials, properties of dielectric materials, presence of slots and airgap and influence of frame materials can be incorporated easily using finite element (FE) analysis software. Further, a much better knowledge of space and the time distribution of the current and magnetic flux, which are important in predicting the performance of the permanent magnet machines, can be obtained from FE analysis [49].

4.2. Method used for finite element analysis

In electromagnetics, the study of magnetics begins with the derivation of the relevant partial differential equation (PDE) for the particular problem using Maxwell's equations. The four Maxwell's equations can be manipulated to produce a general PDE that will apply to a variety of eddy current problems as well as linear and non-linear time and frequency domain magnetic flux modelling problems [50, 51]. Finite element modelling (FEM) technique is

widely used as a numerical method of solving linear and non-linear PDE. The most popular methods of deriving the finite elements are:

(i) Variational approach and

(ii) Galerkin approach.

The variational approach was the first applied to problems in magnetics and occupies a large part of the early literature. This method however was not accurate and there are a large number of practical cases in electrical machinery analysis in which this method either is not known or does not exist. Because of the greater generality of the galerkin approach, this method is commonly used in the present days. The galerkin method, which is a method of weighted residual is applied to the general PDE derived from Maxwell's equation to produce a set of algebraic equations. These equations are then solved to yield a distribution of magnetic vector potentials (MVP) over a cross-section of the domain under study. The equations obtained can be used to solve a variety of problems in magnetics involving linear as well as non-linear analysis. Because of the versatility of the FEM, these equations can also be used to solve the temperature distribution problem with or without a heat source [31].

Finite element analysis also plays an important role in the design-analysis-production cycle. By using FEM, a product's mechanical and electromagnetic behavior can be simulated thus reducing the need for fabrication and testing of numerous prototypes. In addition to reducing the need for costly prototype fabrication and testing, FEM is also used to increase product reliability, identify potential structural problems prior to manufacture, reduce material and manufacturing costs and reduce time in the design-analysis-production cycles through rapid design iterations [52]. The finite element method of analysis software used in this project is provided by MacNeal-Schwendler Corporation (MSC) of USA [53]. The software package has the capabilities of two joint programs namely MSC/XL and MSC/EMAS respectively. In this thesis, the geometry of the uniform airgap and shaped pole machines were translated into

two dimensional finite element meshed models using MSC/XL program and MSC/EMAS performs the analysis.

4.3 Finite element modelling

4.3.1 Geometry and meshing

Finite element analysis involves meshing a structure into discrete entities called elements and grid points. Elements are small portions of a whole structure and are similar to the building blocks. The grid points define the boundaries of each element, and the collection of all grid points represents the geometry of the structure being modeled.

In MSC/XL, the creation of the finite elements can be divided into two classes of operation, one based on geometry and another one based on finite elements. The generation of finite elements can be done in two ways. One way is to create a geometry and then superimpose finite elements upon geometric entities already in place. Another way is to directly define the finite elements, that needs to be created and specify the grid point regions to be occupied by the finite elements. These two classes of operation namely, generating the finite elements based on the geometry and generating finite elements based on the existing finite elements, can be used both separately or in combination.

Different geometric models have different meshing requirements. The following meshing techniques are available:

(i) Parametric meshing,

(ii) Station meshing,

(iii) Delaunay meshing and

(iv) Extrude meshing.

Delaunay meshing technique can be employed to define the number of divisions on all edges of the region to be meshed thus allowing for unequal divisions on opposite sides of the region. The ability to provide unequal divisions is especially useful when a transition of the model from a fine mesh to a coarse mesh is required. The finite element models developed in this thesis uses delaunay meshing that is unique in handling difficult modelling situations [53].

The geometry and finite element meshing of the ¼ model of the 4-pole shaped airgap machine is shown in Figures 4.1. The finite element model of a shaped airgap machine is similar to that of the model developed for the uniform airgap machine, except for the shaping of the airgap profile. Both uniform airgap and shaped pole machines are meshed using an equal number of elements to assure a similar degree of accuracy. It can be seen from Figure 4.1, sufficient number of elements were used in the critical regions to model the machine shape more accurately. Also in order to avoid remeshing of the airgap when the rotor is moved, care was taken to mesh the airgap so that the common sides of the elements of the two layers closest to the stator surface were of equal circumferential length. The finite element models are constructed based on the theoretical model developed in Chapter 2. While creating the finite element model, it must be ensured that the geometry and element mesh density are refined enough to yield accurate and meaningful results. If the results are not accurate enough for a particular design application, then mesh density and/or geometry is modified, until more reasonable and accurate results are obtained.

Airgap flux density is one of the important aspects that influences the torque production mechanism and the operating characteristics of the interior permanent magnet motor. Since details of the airgap flux distributions are of interest in the analysis, fine meshes are employed in the airgap of both uniform and shaped machines. Enlargement of the airgap finite element meshing for a shaped machine is shown in Figure 4.2.

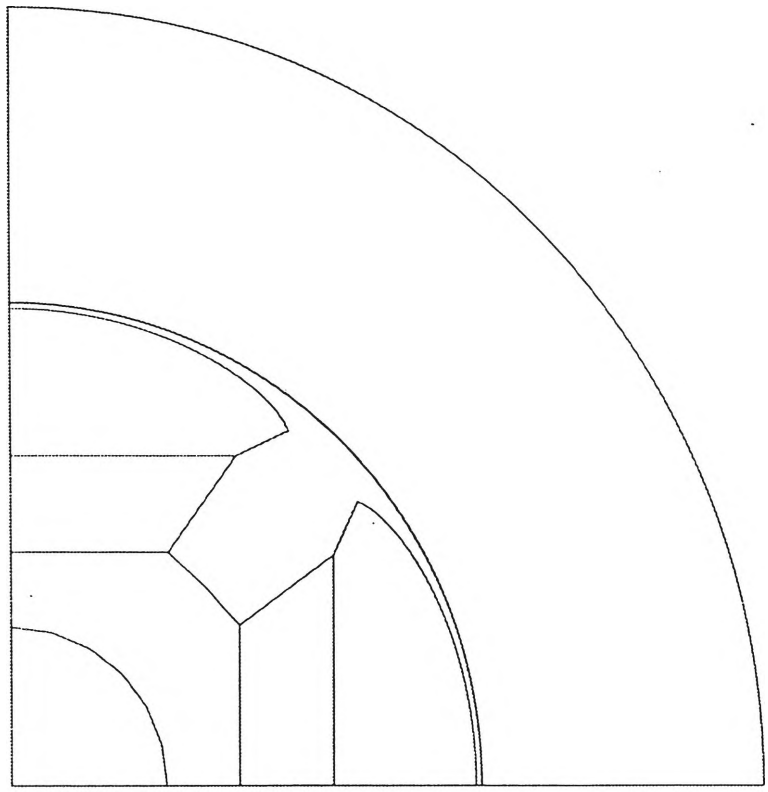

(a) Geometry of the shaped pole machine

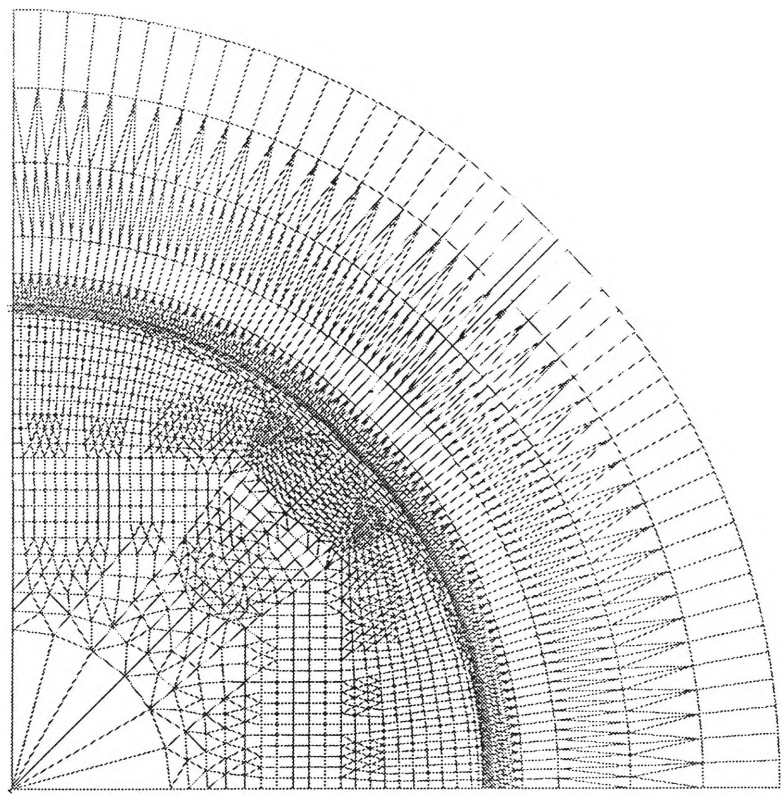

(b) Finite element ¼ model of shaped pole machine

Figure 4.1 Geometry and finite element ¼ model of the 4-pole shaped airgap machine

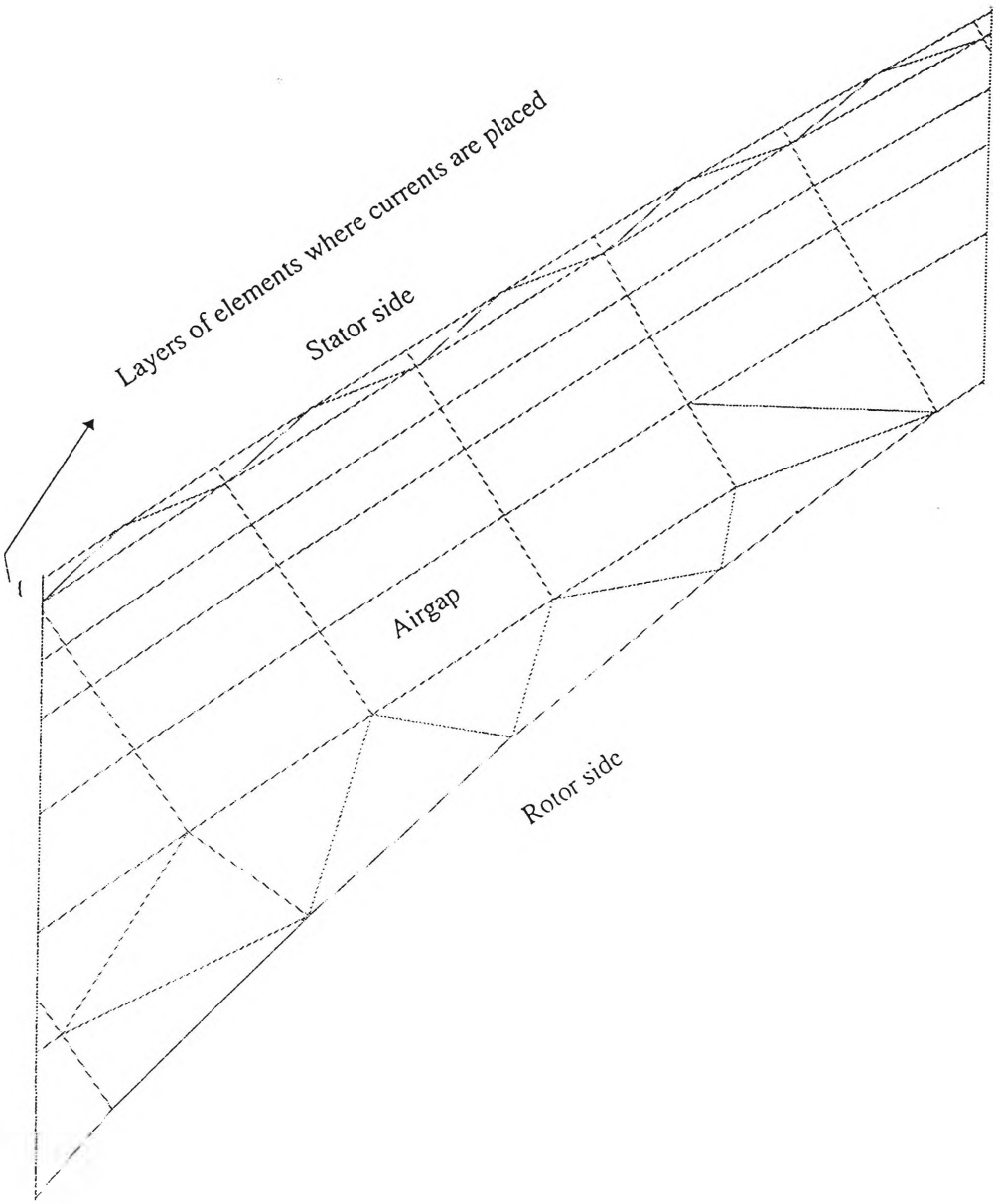

Figure 4.2 Enlarged airgap finite element meshing of the shaped airgap machine

In the finite element models of the machine shown in Figure 4.1, boundary conditions were imposed with the assumptions that the magnetic field outside the stator periphery are negligible. Hence, the outer periphery of stator core was applied with single point constraints setting the magnetic vector potential in the Z-direction to zero. The magnetic vector potential in the Z-direction at both vertical and horizontal boundaries are made dependent on each other using multi point constraints applied along the two boundaries of the ¼ model. The related potentials are made equal in values but opposite in polarity. This is made

possible because of the symmetrical nature of the 4 pole machine. For accurate and more reliable finite element models, certain areas of problems such as errors in connectivity, duplicate grids and elements, inconsistent or reversed element and element distortions are verified using the checking operations available in the finite element software package. The models that are created are then analyzed using the nonlinear static magnetic field solutions, which was the first step towards the performance calculation of the machines.

4.3.2 Hypothetical stator winding distribution

The mathematical model of the interior permanent magnet machine developed in Chapter 2, uses a theoretical stator winding distribution. The values of the stator winding distribution calculated for a prototype machine considered in this thesis is shown in Figure 4.3. The specifications of the prototype machine is given in Appendix B. The winding distribution calculated is then used for the excitation of the slots with appropriate currents. In the finite element model, the windings are distributed in a very thin layer of elements created closer to the stator inner surface and the currents are distributed along that layer. The results shown in Figure 4.3 are obtained from Equation (2.10) of Chapter 2. It can seen from Figure 4.3, that the maximum (peak) value of number of turns is equal to 62, which is calculated using the expression in Equation (2.12) of Chapter 2.

In the mathematical and finite element models, the pole arc angle is reduced from 180° thus resulting in an interpolar region. The pole arc angle of the existing prototype machine, is equal to 154°. In the mathematical model, the windings distributed in the interpolar regions are assumed to produce useful flux which crosses the airgap. In a finite element model, the flux produced by the currents in the interpolar region are not strong enough because of the very large reluctance path, thus resulting in a smaller amount of useful flux production when compared to the flux production in a mathematical model. Hence the number of turns used in finite element models are squeezed, in such a way that there is no winding distribution in the interpolar regions and still able to produce

the same amount of useful flux when compared to the mathematical model. As before, the values of the squeezed sinusoidal winding distribution can be obtained using Equation(2.10) of Chapter 2 and the plot of the resultant winding distribution at each angle is shown in Figure 4.3. The values of hypothetical stator windings spread over the pole arc angle of 180° and squeezed stator winding distribution are given in Table C1 of Appendix C.

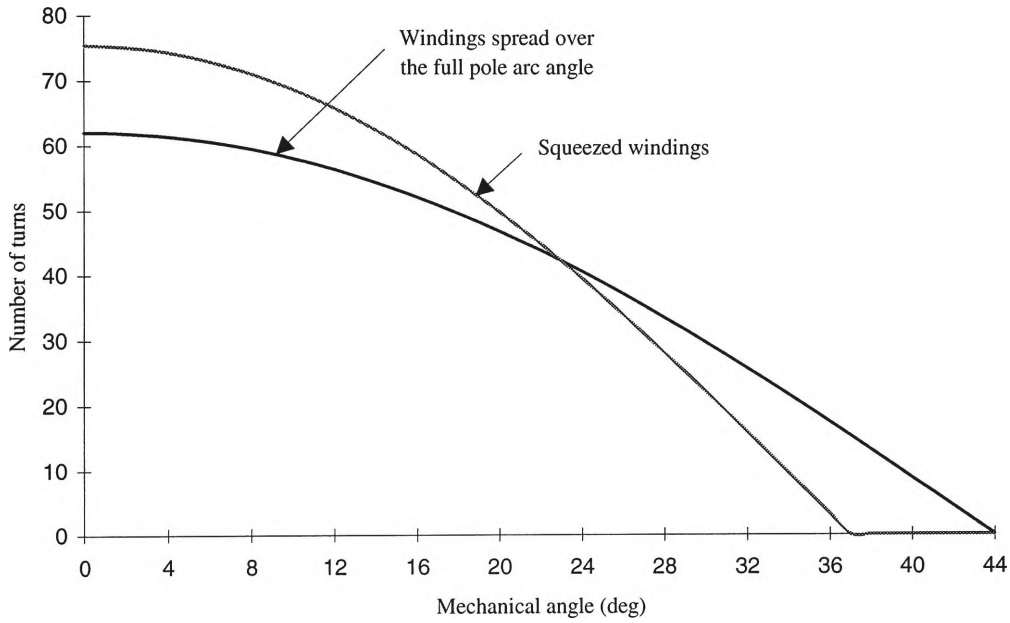

Figure 4.3 Stator turns distribution over the full pole arc angle and turns distribution of squeezed hypothetical stator winding

4.4 Summary

This chapter discussed the finite element method that has been employed to analyse the behaviour of IPM machines. The finite element software used in this thesis along with the basic concepts and principle involved in it were also described in this chapter. The procedures required for the modelling of the IPM machines using finite element when compared with the mathematical model developed in previous chapters have also been presented in this chapter.

CHAPTER 5

APPLICATION OF MATHEMATICAL MODEL AND FINITE ELEMENT SIMULATION MODELS

5.1 Introduction

In Chapters 2 and Chapters 4, the mathematical and finite element models were developed for the design optimization of the interior permanent magnet motor. The application of these models to a prototype machine to evaluate the performance of the machine is presented in this chapter. Some of the quantities such as quadrature axis inductance and torque, which are important in assessing the performance of the motor, especially where vector control is employed are also calculated in this chapter. The q-axis inductance for a uniform and shaped airgap machine is compared where good agreement is found between the theoretical and finite element results.

5.2 Theoretical results

5.2.1 Comparison of q-axis inductances

The mathematical model developed in Chapter 2 is now applied to the considered prototype machine. The first step that is required is to calculate the value of maximum (peak) number of turns related to the mathematical model. This is carried out by using the Equation (2.12) derived in Chapter 2 which is found to be equal to 62. For different pole arc angles, the values of q-axis inductance for both uniform and shaped airgap machines are calculated using the expressions in Equations (3.5) and (3.10) of Chapter 3 as shown in Table 5.1. The percentage reduction of q-axis inductance between the shaped airgap machine and uniform airgap machines is also shown in Table 5.1.

pole arc angle (deg)	Lq Uniform (H)	Lq Shaped (H)	Percentage reduction
180	0.0908	0.0385	57.56
178	0.0888	0.0385	56.61
176	0.0868	0.0385	55.67
174	0.0848	0.0384	54.72
172	0.0827	0.0383	53.76
170	0.0807	0.0381	52.81
168	0.0787	0.0379	51.86
166	0.0768	0.0377	50.90
164	0.0748	0.0374	49.94
162	0.0728	0.0371	48.99
160	0.0708	0.0368	48.03
158	0.0689	0.0365	47.08
156	0.0669	0.0361	46.12
154	0.0650	0.0357	45.17
152	0.0631	0.0352	44.22
150	0.0612	0.0347	43.27
148	0.0593	0.0342	42.32
146	0.0575	0.0337	41.37
144	0.0557	0.0332	40.43
142	0.0538	0.0326	39.49
140	0.0520	0.0320	38.56
138	0.0503	0.0314	37.63
136	0.0485	0.0307	36.70
134	0.0468	0.0301	35.78
132	0.0451	0.0294	34.87
130	0.0434	0.0287	33.95
128	0.0418	0.0280	33.05
126	0.0402	0.0273	32.15
124	0.0386	0.0265	31.26
122	0.0370	0.0258	30.38
120	0.0355	0.0250	29.50

Table 5.1 Comparison of q-axis inductance for uniform and shaped airgap machines

The selection of optimum pole arc angle of an IPM machine depends on various factors such as magnet to magnet leakage flux, stator leakage flux and average torque production. A large reduction in pole arc angle results in a saturation of teeth, pole pieces and a decrease in average torque produced. The range of pole arc angles for which the results are calculated is from 180° to 120°. The pole arc angle for the prototype machine is equal to 154°, which is considered as an adequate value. From the mathematical model, as seen in Table 5.1, at the

particular pole arc angle of 154°, the q-axis inductance for uniform and shaped airgap machine is equal to 0.065H and 0.0357H. The percentage reduction for the q-axis inductance of the uniform and shaped airgap machine is equal to 45.17%. A plot of the q-axis inductance values obtained from Table 5.1 is shown in Figure 5.1.

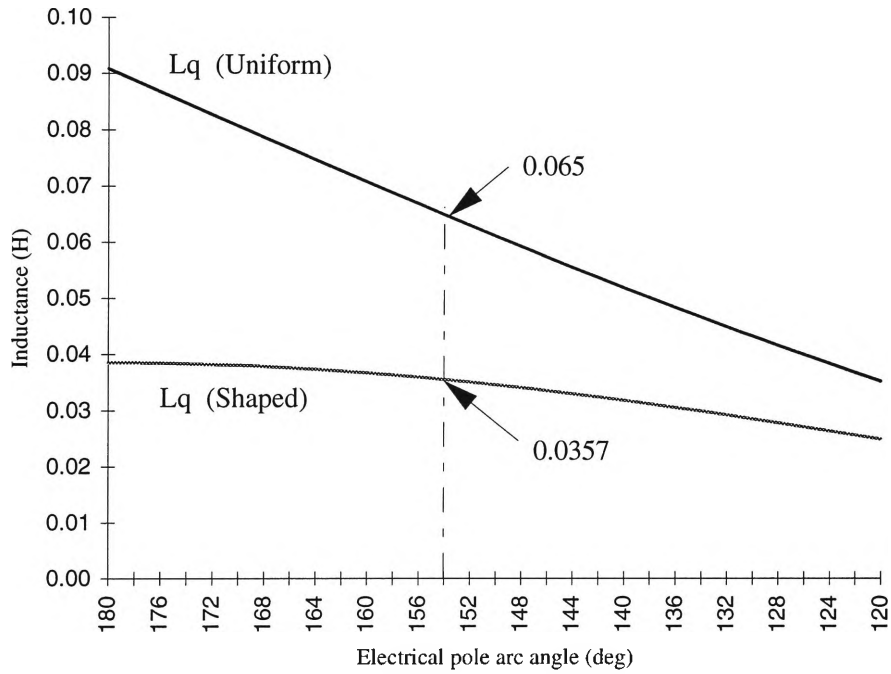

Figure 5.1 Comparison of q-axis inductances

Figure 5.1 shows the expected trend in the levels of inductance for the shaped and uniform airgap machine. The value of inductance is smaller for a shaped airgap machine when compared to a uniform airgap machine for all pole arc angles. As seen from the Figure 5.1, the differences in the quadrature axis inductance between the two machines at smaller pole arc angles is low. This characteristic is useful in considering a reasonably higher pole arc angle in a shaped airgap machine when a lower value of q-axis inductance is required. The plot representing the ratio of q-axis inductance of shaped airgap machine to q-axis inductance of uniform airgap machine with respect to pole arc angle ranging from 180° to 120° is shown in Figure 5.2. It can be seen from Figure 5.2, that the percentage reduction in q-axis inductance of the shaped airgap machine

when compared to a uniform airgap machine is less for lower pole arc angles. As seen from Figure 5.1, for a uniform airgap machine having a cylindrical rotor construction, the value of q-axis inductance is equal to 0.0908H.

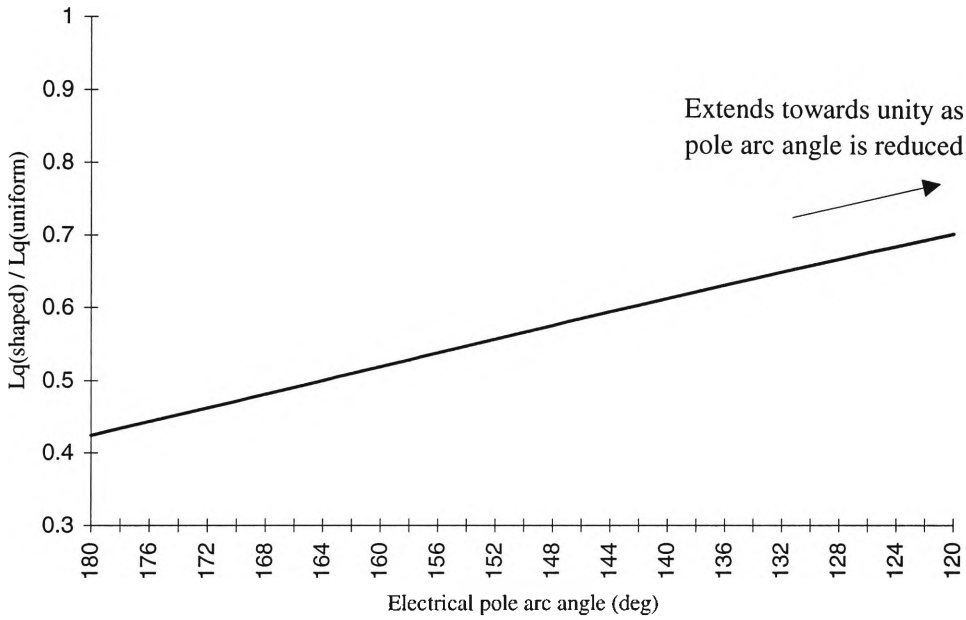

Figure 5.2 Ratio of q-axis inductance of shaped and uniform airgap machine Vs electrical pole arc angle

5.2.2 Machine with cylindrical rotor construction

For verifying the mathematical model, the q-axis inductance can be calculated for a prototype machine by considering the developed diagram as shown in Figure 5.3a. For simplicity, the rotor is considered to be cylindrical in structure. As seen from Figure 5.3a, the existing prototype machine uses a double layer winding and the coils are short pitched by two slots. The winding distribution of a single phase in the stator slots are used for the calculation of the inductance of the machine. The MMF distribution of the winding placed in the slots 17 to 30 is shown in Figure 5.3b. The height of each MMF step equals the number of ampere-conductors $2N_c I$ in the slot, where N_c is the number of turns in each coil and I is the current in the coil. The flux linkage in the machine can be calculated by taking the product of flux density produced by the number of turns

over the surface area.

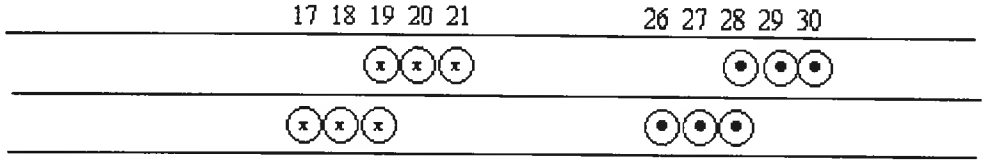

(a) Developed sketch of slots with winding

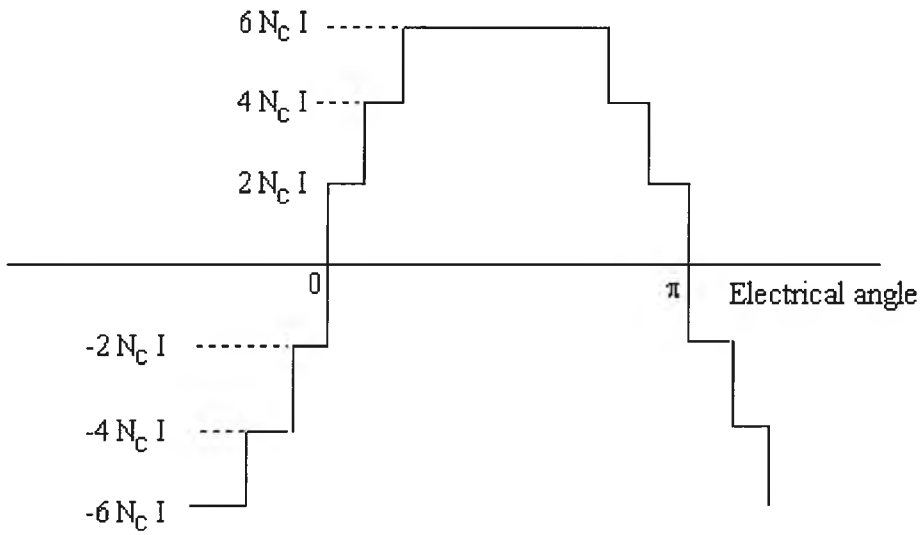

(b) MMF distribution

Figure 5.3 MMF distribution for the existing prototype machine

As seen in Figure 5.3, the total MMF for a single pole of the machine consists of three levels having a peak value equal to $6N_c I$ ampere turns. The flux linkage for each level can be calculated by using the standard procedure. The inductance is given by the ratio of flux linkage to the current in the coil and the value is found to be equal to 0.0934H. Since the prototype machine is considered to be having a cylindrical rotor construction, the pole arc angle is equal to 180°. The value of inductance obtained is comparable to the result obtained from the mathematical model, which is equal to 0.0908H.

5.3 Finite element results

5.3.1 Field analysis of uniform airgap machine

Two dimensional finite element models are analysed using the nonlinear static magnetic analysis solution of MSC/EMAS. Output results available from the analysis are magnetic flux density for each element of the model, magnetic vector potential at every grid point of the model, stored magnetic energy and stored magnetic co-energy. These results can be used to calculate the required quantities such as inductances and torque.

In order to calculate the inductance, the radial component of flux density in the airgap due to the stator current is required. The finite element model was developed accordingly as discussed in Chapter 4. The radial component of airgap flux density obtained by using a cutpath along the airgap in the finite element model for the uniform airgap machine having hypothetical stator winding distribution is shown in Figure 5.4. The arrow plot of full vector component of flux density distributions obtained from finite element model is shown in Figure 5.5. These values are used in the calculation of the q-axis inductance as shown in Table D1 of Appendix D.

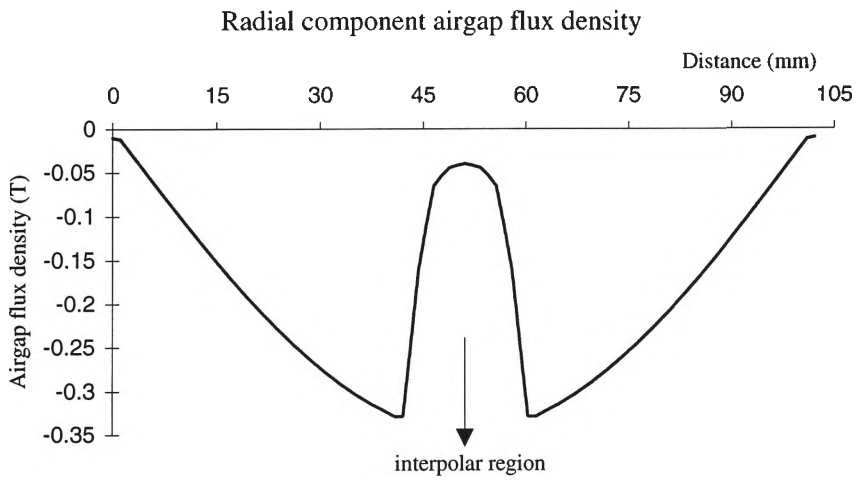

Figure 5.4 Radial component airgap flux density for the uniform airgap machine having hypothetical windings in the stator

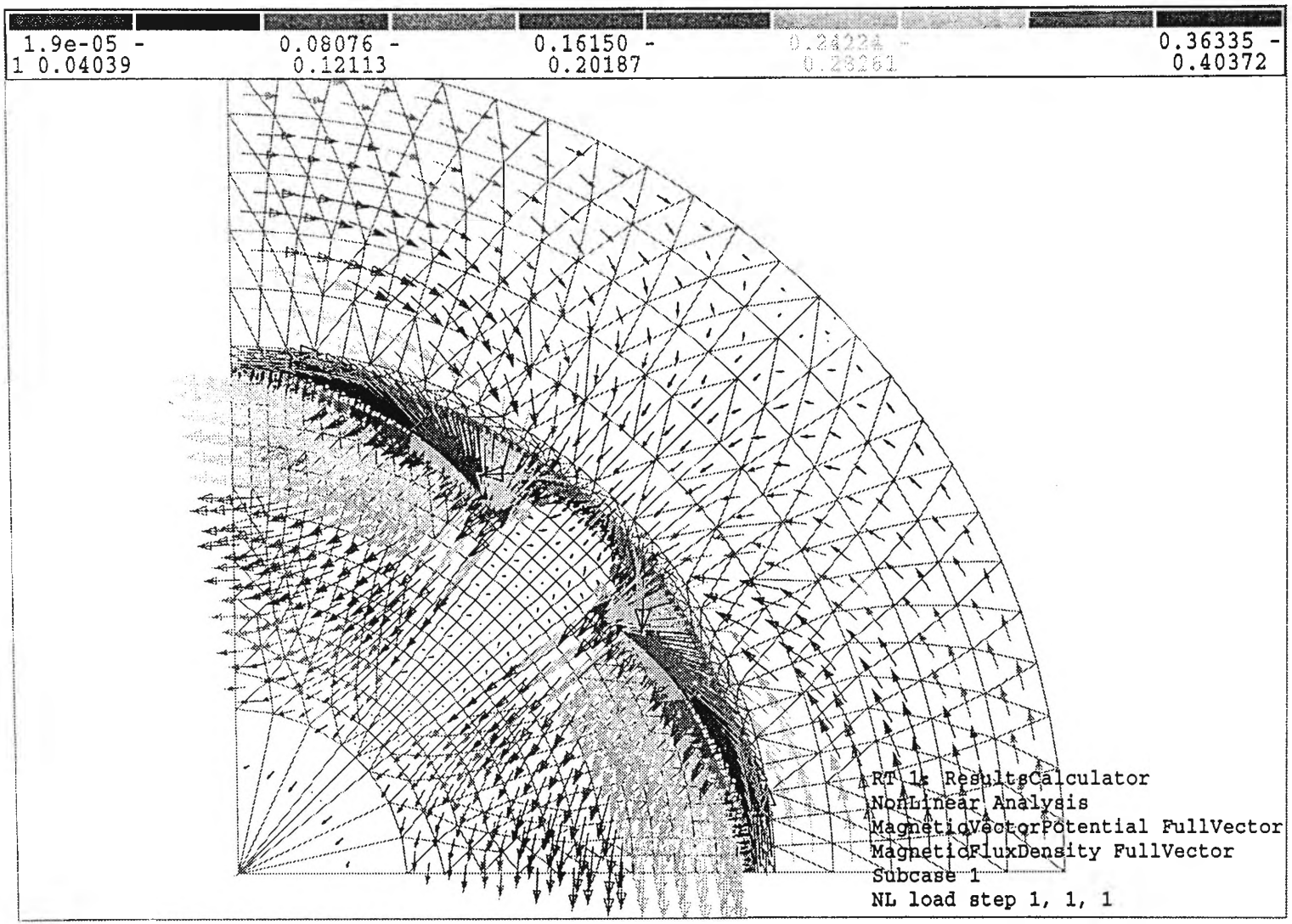

Figure 5.5 Arrow plot of full vector component of flux density distribution for the uniform airgap machine having hypothetical stator windings spread over the full pole arc angle

It can be seen from Table D1 of Appendix D, the calculated value of quadrature axis inductance for a uniform airgap machine having a hypothetical stator winding distribution is equal to 0.0477H. This value obtained from finite element model is less when compared to the results obtained from the mathematical model. As discussed before, one significant reason for this difference in q-axis inductance is the windings present along the interpolar regions. This reasoning can be further proved by squeezing the number of turns such that there are no coils present in the interpolar region as discussed in section 4.3.2 of Chapter 4. The radial component of airgap flux density that is obtained by using a cutpath along the airgap profile in the finite element model having a squeezed stator winding distribution is shown in Figure 5.6. It can be seen from Figure 5.6, the maximum value of radial component airgap flux density has increased to a value of about 0.45T when compared to the maximum value (0.35T) obtained for the stator winding distributed over the full pole arc angle shown in Figure 5.4. The arrow plot of full vector component of flux density distribution obtained from finite element model having squeezed stator winding distribution is shown in Figure 5.7. As before, these values are used in the calculation of the q-axis inductance shown in Table D2 of Appendix D.

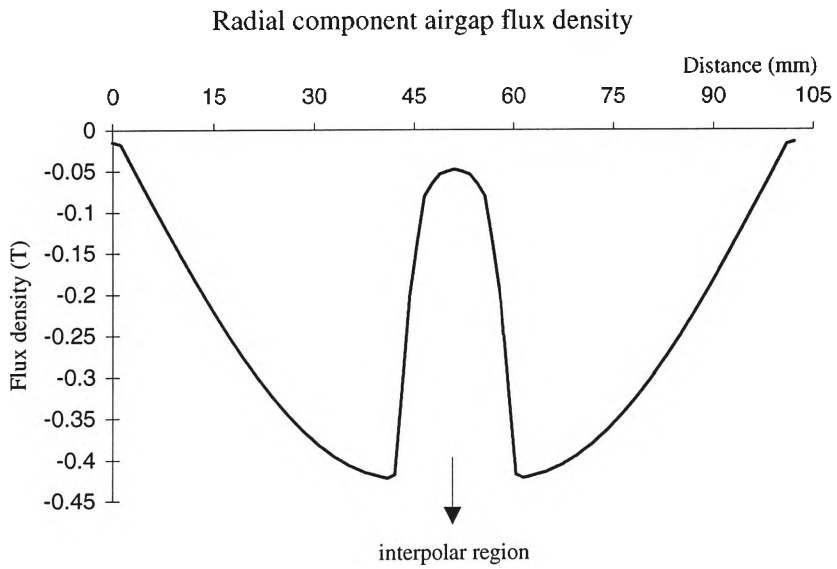

Figure 5.6 Radial component airgap flux density for the uniform airgap machine having squeezed hypothetical windings in the stator

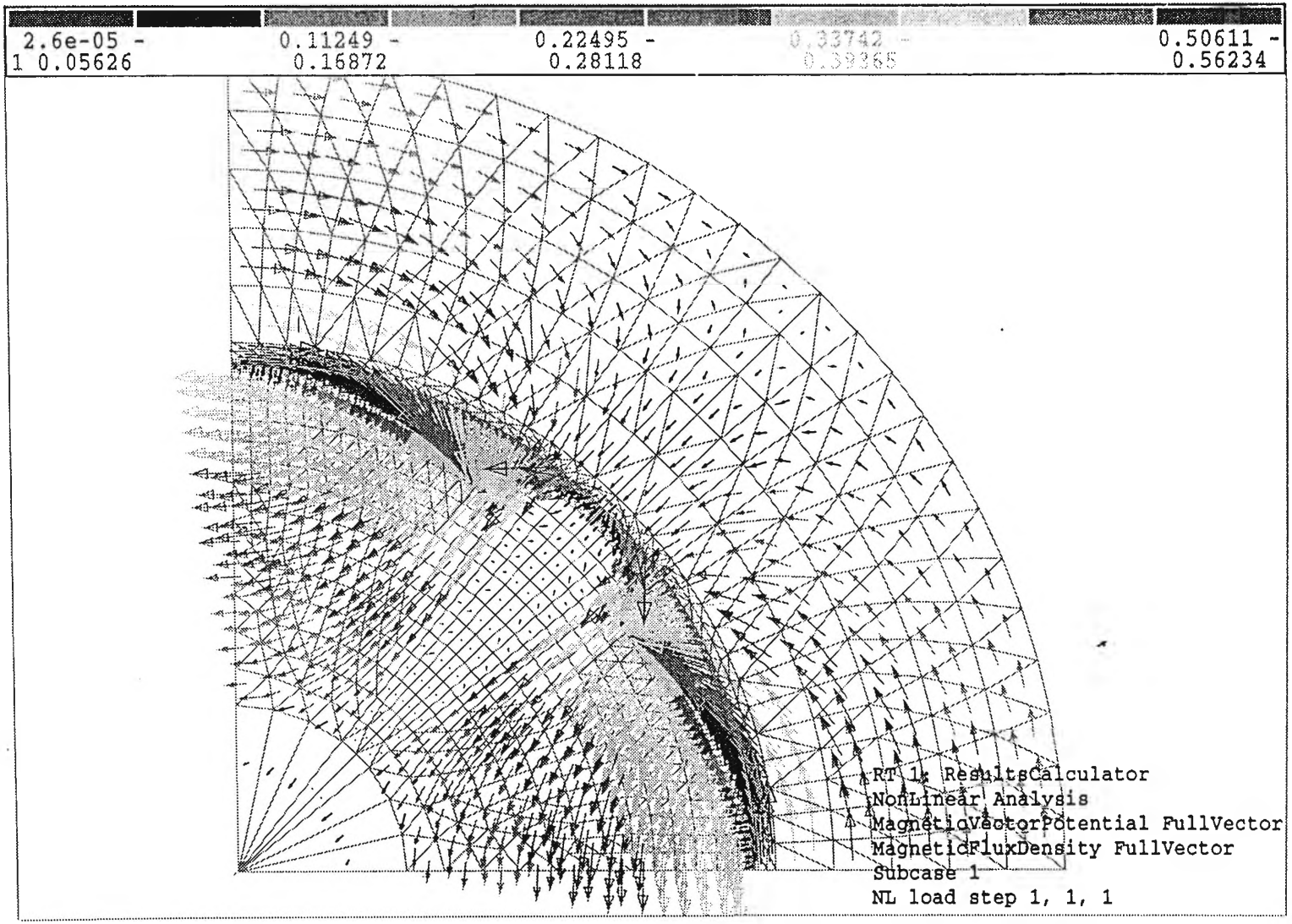

Figure 5.7 Arrow plot of full vector component of flux density distribution for the uniform airgap machine having squeezed hypothetical stator windings

The value of q-axis inductance for the uniform airgap machine having a squeezed hypothetical winding distribution is found to be equal to 0.0659H as seen in Table D2 of Appendix D. This value is closer to the value of inductance (0.0650H) calculated using the mathematical model for the same machine. The validity of the squeezed winding distribution is also further proved by analyzing the results from the finite element model. The menu bar displayed at the top of the full vector component flux plots shown in Figures 5.5 and 5.7 gives the range of the flux density levels that exists throughout the machine. It can be seen that the maximum value of flux density for the uniform airgap machine having a hypothetical winding distribution is equal to 0.40T, which is less when compared to the machine having squeezed stator winding distribution which is equal to 0.56T.

5.3.2 Field analysis of shaped airgap machine

In Section 5.3.1, the analysis of the uniform airgap machine developed using a mathematical model is carried out on a 2 dimensional finite element model. The same procedure is also used for the analysis of the shaped airgap machine. The radial component airgap flux density which is obtained by using a cutpath along the airgap profile in the finite element model of the shaped airgap machine having a hypothetical stator winding distribution spread over the full pole arc angle of 180° and squeezed hypothetical stator winding distribution are shown in Figures 5.8 and 5.9. The effect of shaping of the airgap profile on the airgap flux density can be seen from both the figures. Also it can be seen from Figure 5.9, the maximum value of radial component airgap flux density has increased to a value of about 0.25T when compared to the maximum value (0.18T) obtained for the stator winding distribution spread over the full pole arc angle of 180° as shown in Figure 5.8. The arrow plot of flux density distributions near the interpolar region and line contour plot from grid results of the finite element model of the shaped airgap machine are shown in Figures 5.10 and 5.11 respectively. As in the case of the uniform airgap machine, the values of radial

component airgap flux density are used in the calculation of the q-axis inductance. Tables D3 of Appendix D shows the calculation of q-axis inductance for the shaped airgap machine having squeezed stator windings.

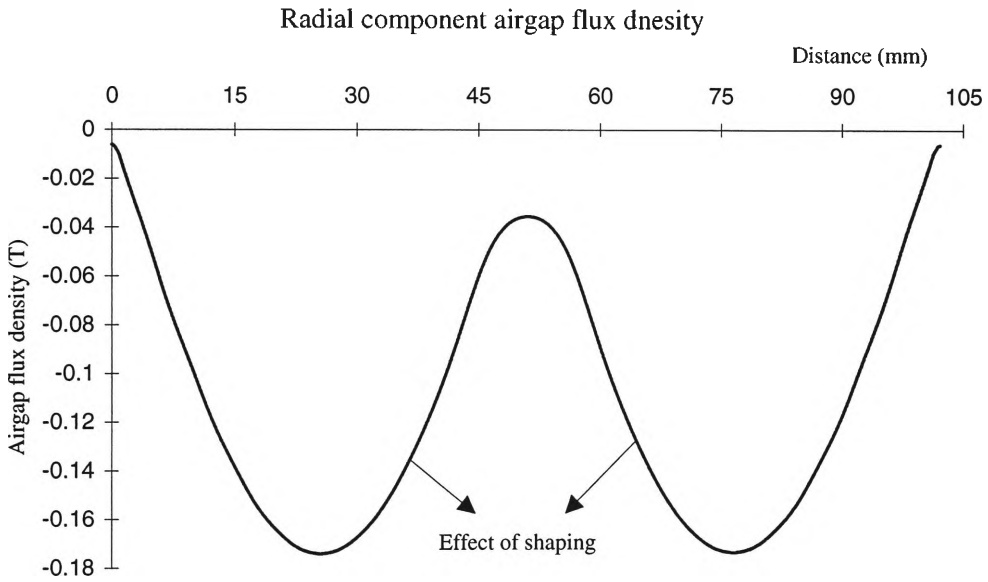

Figure 5.8 Radial component airgap flux density for the shaped airgap machine having hypothetical windings in the stator

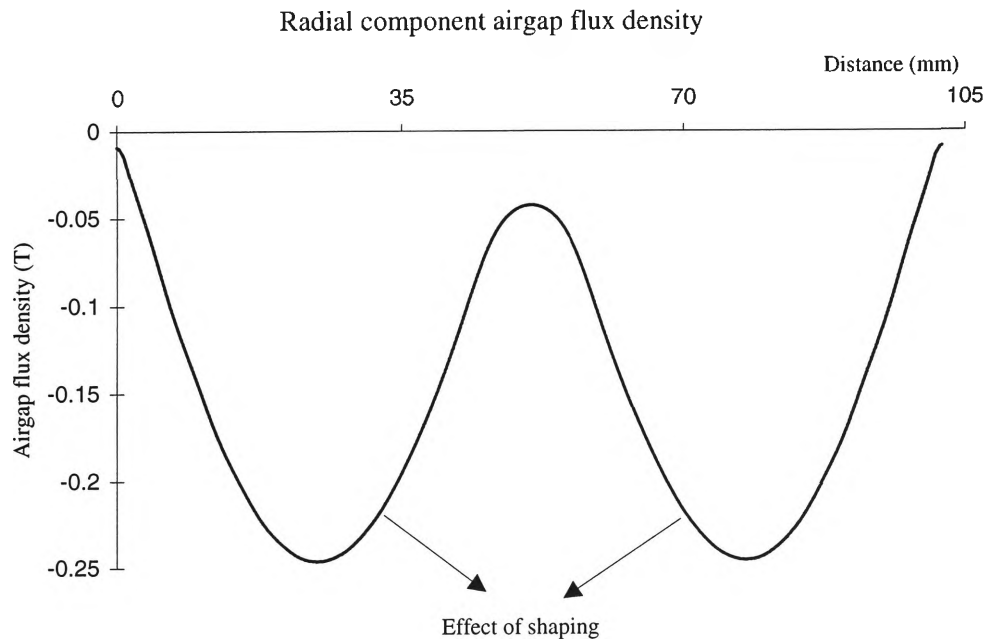

Figure 5.9 Radial component airgap flux density for the shaped airgap machine having squeezed hypothetical windings in the stator

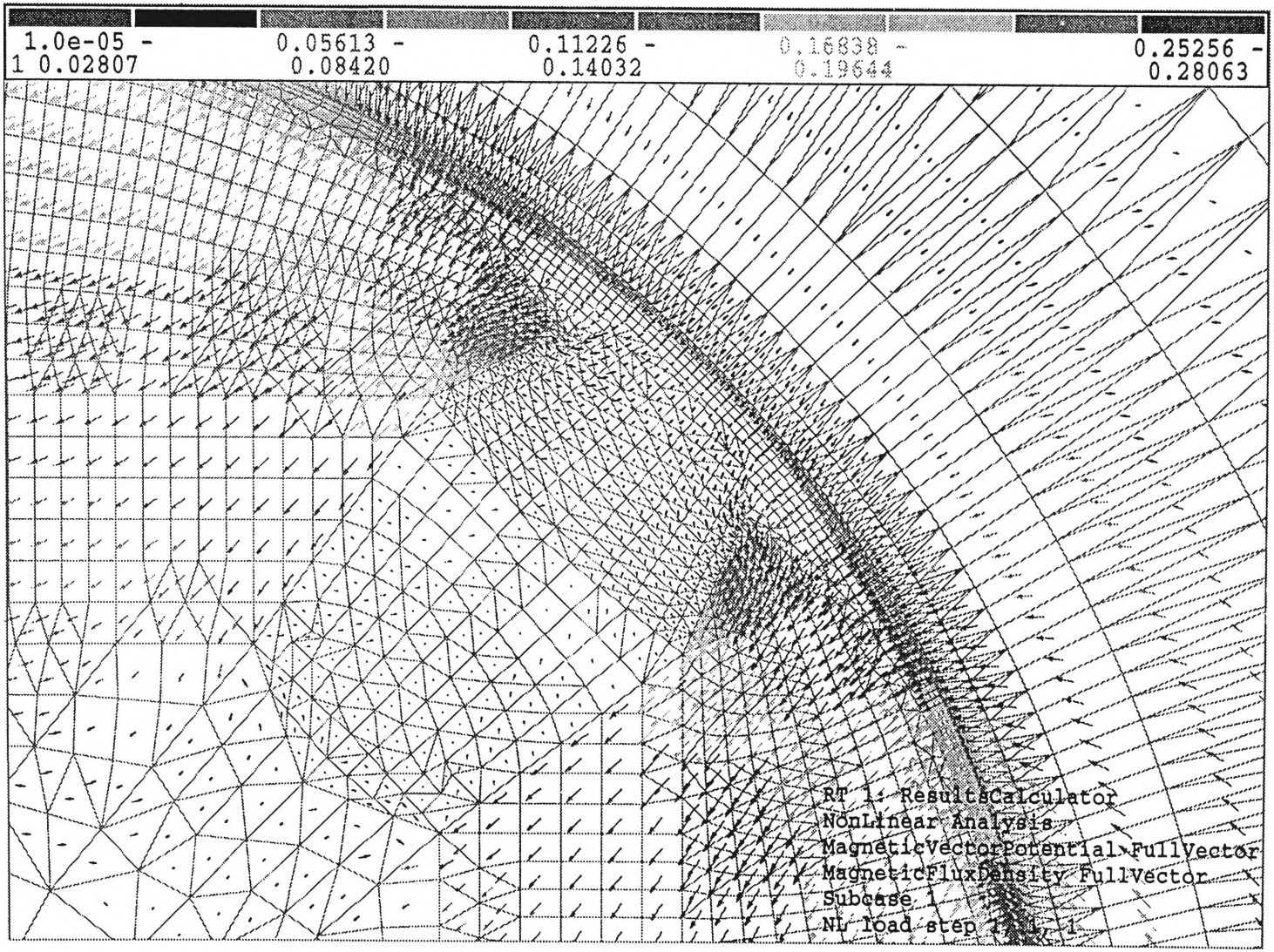

Figure 5.10 Arrow plot of full vector component of flux density distribution for the shaped airgap machine having squeezed hypothetical stator windings

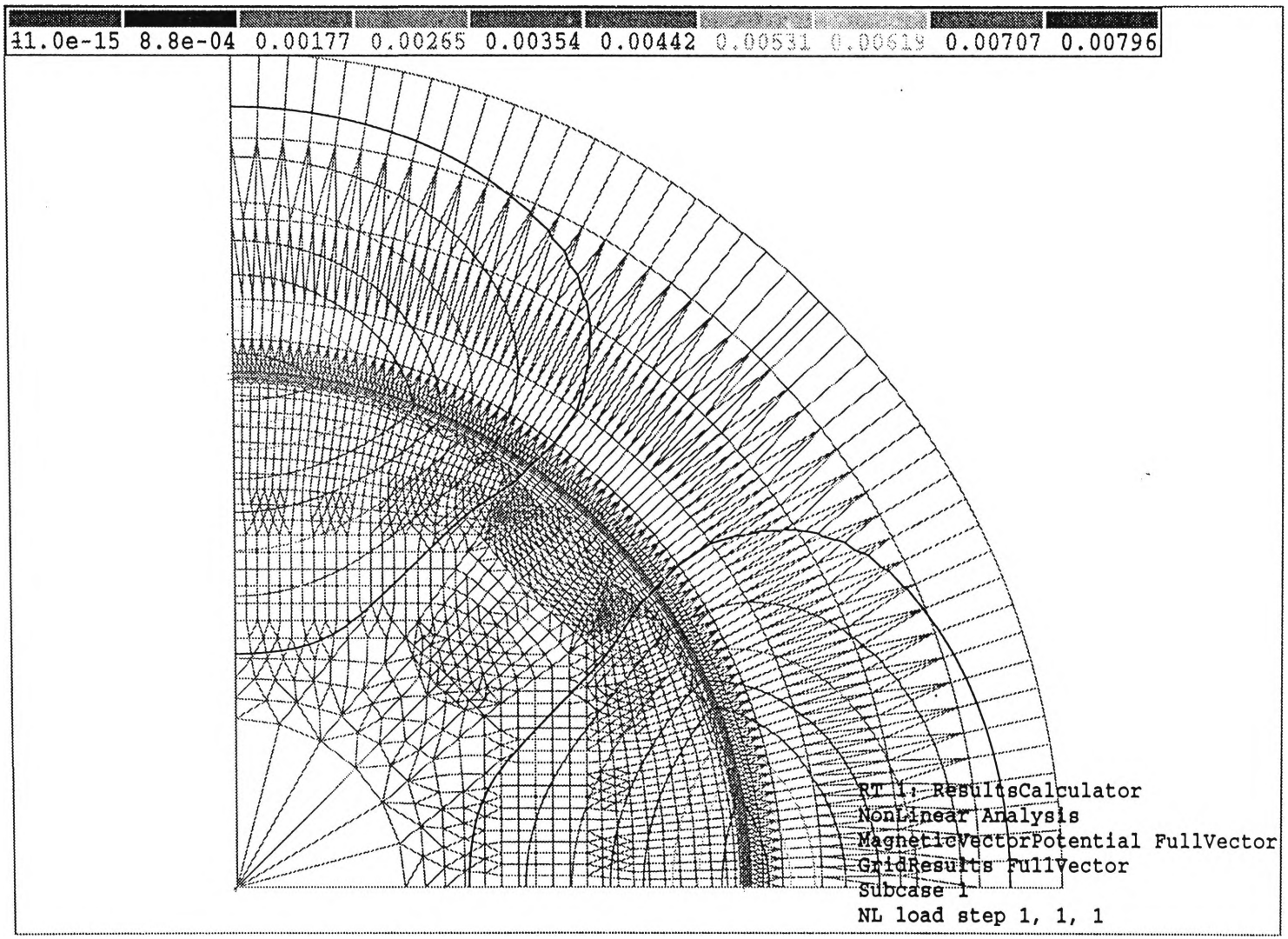

Figure 5.11 Contour plot of grid results for the shaped airgap machine having squeezed hypothetical stator windings

The value of q-axis inductance for the shaped airgap machine having a squeezed hypothetical winding distribution is found to be equal to 0.0385H as shown in Table D3 of Appendix D. This value is closer to the value of inductance (0.0357H) calculated using the mathematical model for the same machine. From the menu bar displayed at the top of the full vector component flux plot for shaped airgap machine having squeezed hypothetical stator winding distribution, shown in Figure 5.10, it can be seen that the maximum value of flux density is equal to 0.39T. From all the finite element models, the maximum value of the flux density is well below the saturation limits of the steel. The flux flow in the shaped airgap machine is obtained from the grid results of the shaped airgap machine finite element model, which can be seen from Figure 5.11.

5.4 Comparison of theoretical and finite element simulation results

The results obtained from finite element modeling and theoretical modeling are compared in Table 5.2. The second row in Table 5.2, gives the values of the quadrature axis inductance for the uniform and shaped airgap machines obtained from the theoretical model. When analyzing the results obtained from the theoretical model, it can be seen that there is a reduction of about 45% in the quadrature axis inductance for the shaped airgap machine when compared to the uniform airgap machine. The reduction of q-axis inductance is very useful in vector control of PM motors as discussed in earlier chapters. Practically the value of inductance is affected by the level of current because of the saturation effects. The q-axis inductance computed from finite element model is obtained by considering a peak rated current of 6A. In Table 5.2, there are two results obtained from the finite element models. One result in last row gives the values of q-axis inductance calculated for the considered prototype machine, from past studies [10]. The other result is the values calculated from the finite element model having a hypothetical stator winding distribution used for the mathematical model. As seen there is a reduction of about 41% in the q-axis

inductance of the shaped airgap machine when compared to the uniform airgap machine. The percentage reduction between the shaped and uniform airgap machine from previous research is around 33%. The difference in the percentage reduction between the two finite element results can be attributed to the assumptions that are used in the mathematical model. One of the primary assumptions being the winding distribution for the machine leading to a more general and simpler mathematical expressions of the relevant design parameters. From Table 5.2, it can also be seen that there is a good agreement between the results obtained from theoretical model and finite element models.

Method of calculation	Uniform airgap machine L_q (H)	Shaped airgap machine L_q (H)
Theoretical results (Hypothetical winding distribution)	0.0650	0.0357
Finite element results (Hypothetical winding distribution)	0.0659	0.0385
Finite element results (Past studies)	0.0661	0.0428

Table 5.2 Quadrature axis inductances

5.5 Summary

The application of the mathematical models and finite element models on a prototype machine to evaluate the performance of the machine was presented. The q-axis inductance, which is important in assessing the performance of the motor, especially where vector control is employed is calculated in this chapter. The q-axis inductance for a uniform and shaped airgap machine from both theoretical and finite element models are also compared and good agreement in results are found between them.

CHAPTER 6

DESIGN AND ANALYSIS OF A 5.5kW MACHINE

6.1 Introduction

In Chapter 5, the application of mathematical and finite element models were undertaken in relation to an existing prototype machine. These models developed can be easily applied to other interior permanent magnet (IPM) machines having different specifications. The analysis of an IPM motor to be built using a standard 5.5kW induction motor frame is presented in this chapter. The values of q-axis inductance for both the uniform airgap and shaped airgap machines are calculated and compared. The validity of the models are further tested by carrying out finite element analysis on these machines.

6.2 Mathematical model

6.2.1 Calculation and comparison of q-axis inductances

The mathematical model developed in Chapter 2 is applied to the prototype machine considered. The specifications of the prototype machine are given in Appendix E. The maximum (peak) number of turns related to the mathematical model is calculated using the Equation (2.12) of Chapter 2 and is found to be equal to 71. The q-axis inductance expressions of Equations (3.5) and (3.10) of Chapter 3 are used for the calculation of inductance for both uniform and shaped airgap machines. Table 6.1 shows the calculated values of inductance for pole arc angles ranging from 120° to 180°. The percentage reduction of q-axis inductance of the shaped airgap machine in comparison to the uniform airgap machine is also shown in Table 6.1.

As discussed in section 5.2.1 of Chapter 5, a pole arc angle of 154° is found to be adequate for the considered prototype machine. From the mathematical

model, as seen in Table 6.1, the value of q-axis inductance for uniform and shaped airgap machines at a pole arc angle of 154° is equal to 0.1066H and 0.0584H. There is a reduction of about 45% in the q-axis inductance of the shaped airgap machine when compared to a uniform airgap machine. A plot of the q-axis inductance for the shaped and uniform airgap machine obtained from the values in Table 6.1 is shown in Figure 6.1.

pole arc angle (deg)	Lq Uniform (H)	Lq Shaped (H)	Percentage reduction
180	0.1488	0.0632	57.56
178	0.1455	0.0631	56.61
176	0.1422	0.0631	55.67
174	0.1389	0.0629	54.72
172	0.1356	0.0627	53.76
170	0.1323	0.0625	52.81
168	0.1291	0.0621	51.86
166	0.1258	0.0618	50.90
164	0.1226	0.0613	49.94
162	0.1193	0.0609	48.99
160	0.1161	0.0603	48.03
158	0.1129	0.0598	47.08
156	0.1097	0.0591	46.12
154	0.1066	0.0584	45.17
152	0.1034	0.0577	44.22
150	0.1003	0.0569	43.27
148	0.0973	0.0561	42.32
146	0.0942	0.0552	41.37
144	0.0912	0.0543	40.43
142	0.0883	0.0534	39.49
140	0.0853	0.0524	38.56
138	0.0824	0.0514	37.63
136	0.0795	0.0504	36.70
134	0.0767	0.0493	35.78
132	0.0739	0.0482	34.87
130	0.0712	0.0470	33.95
128	0.0685	0.0459	33.05
126	0.0659	0.0447	32.15
124	0.0633	0.0435	31.26
122	0.0607	0.0423	30.38
120	0.0582	0.0410	29.50

Table 6.1 Comparison of q-axis inductance for uniform and shaped airgap machine

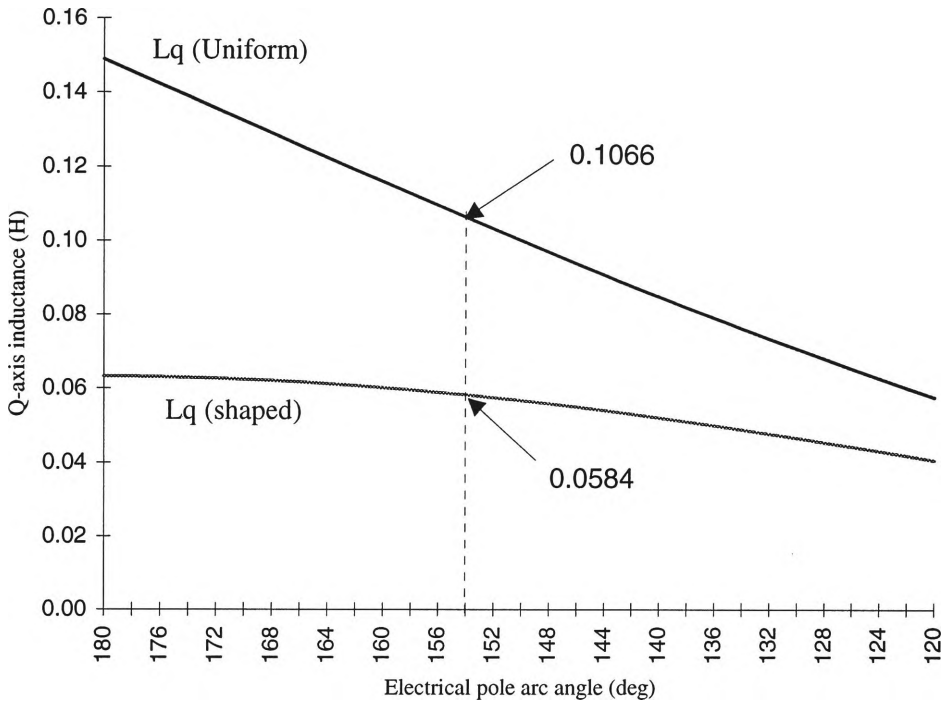

Figure 6.1 Comparison of q-axis inductances

6.2.2 Prototype machine with cylindrical rotor construction

The inductance of the actual machine with discrete windings can be calculated by considering the developed stator winding diagram shown in Figure 6.2a. For simplicity, the rotor is considered to be cylindrical in structure. There is a total of 48 stator slots present in the prototype machine. The breadth and pitch factors of the winding with respect to the fundamental and fifth space harmonics for different coil spans are shown in Table 6.2.

Harmo-nic	Breadth factor	Pitch factor				Winding factor			
		Full pitch	11/12 pitch	5/6 pitch	3/4 pitch	Full pitch	11/12 pitch	5/6 pitch	3/4 pitch
First	0.9577	1	0.9914	0.9659	0.9239	0.9577	0.9495	0.9250	0.8848
Fifth	0.2053	1	0.7934	0.2588	-0.3827	0.2053	0.1629	0.0531	-0.0786

Table 6.2 Breadth and pitch factors

The fractional pitch for the machine decreases the harmonic content of both voltage and MMF waves. But there is also a reduction in the fundamental voltage produced by the winding. Hence the choice of the coil pitch usually depends on the amount of reduction present in both harmonics and the fundamental components. As it can be seen from Table 6.2, that the winding factor of 0.9250 corresponding to a coil pitch of 5/6 seems to be suitable. The MMF distribution of the winding placed in slots 26 to 37 is shown in Figure 6.2b, which consists of series of steps with a peak value equal to $8N_cI$ ampere turns, where N_c is the number of turns in each coil and I is the current in the coil. By using the same procedure used in section 5.2.2 of Chapter 5, on the previous prototype machine, the inductance calculated for the new machine is found equal to 0.154H. This value is comparable to the result obtained from the mathematical model of uniform airgap machine from Table 6.1, at the pole arc angle of 180°, which is equal to 0.1488H.

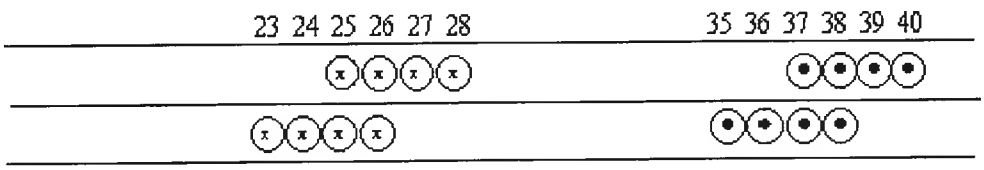

(a) Developed sketch of slots with winding

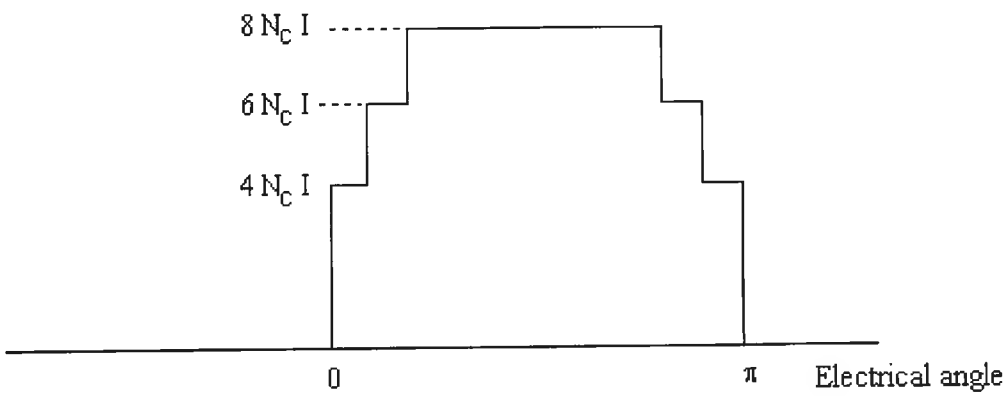

(b) MMF distribution

Figure 6.2 MMF distribution for the prototype machine having 48 slots.

6.3 Finite element model

The results of q-axis inductance calculated from the mathematical model is verified by using finite element modelling. The geometry of the full model of the 4-pole prototype machine with uniform airgap profile and shaped airgap profile is shown in Figure E2 and Figure E3 of Appendix E. The shaping of the airgap profile is accomplished using Equation (2.8) derived in Chapter 2. The calculated values of the shaped airgap lengths used in finite element model is shown in Table F1 of Appendix F.

To calculate the quadrature axis inductance, phase A winding of the finite element model was excited with the rated current. Thus, currents in the other two phases were set equal to zero and the magnet excitation was also set equal to zero. The radial component airgap flux density for the uniform airgap machine and shaped airgap machine is shown in Figure 6.3 and Figure 6.4 respectively. It can be seen from Figures 6.3 and 6.4 that the maximum value of flux density for the shaped airgap machine is reduced to a value of 0.75T when compared to the maximum value of the uniform airgap machine which is equal to 0.95T. The quadrature axis flux that is established due to the stator winding is evident from the flux plots shown in Figure 6.5 and Figure 6.6 for the uniform airgap machine and shaped airgap machines. In these flux plots, the menu bar at the top of the figures indicates the various flux density levels assigned to the arrows. It also gives the range of the flux density levels that exists throughout the machine. The flux due to stator windings, entering the rotor pole, experiences a higher reluctance in the direct axis path due to low permeability of the magnet spaces and attempts to pass through the pole edges crossing the airgap via the stator teeth to the adjacent pole. The q-axis inductance can be calculated from the values of radial component of airgap flux density for both uniform and shaped airgap machine. The values of q-axis inductances for uniform airgap and shaped airgap machines are found to be equal to 0.0931H and 0.0623H respectively.

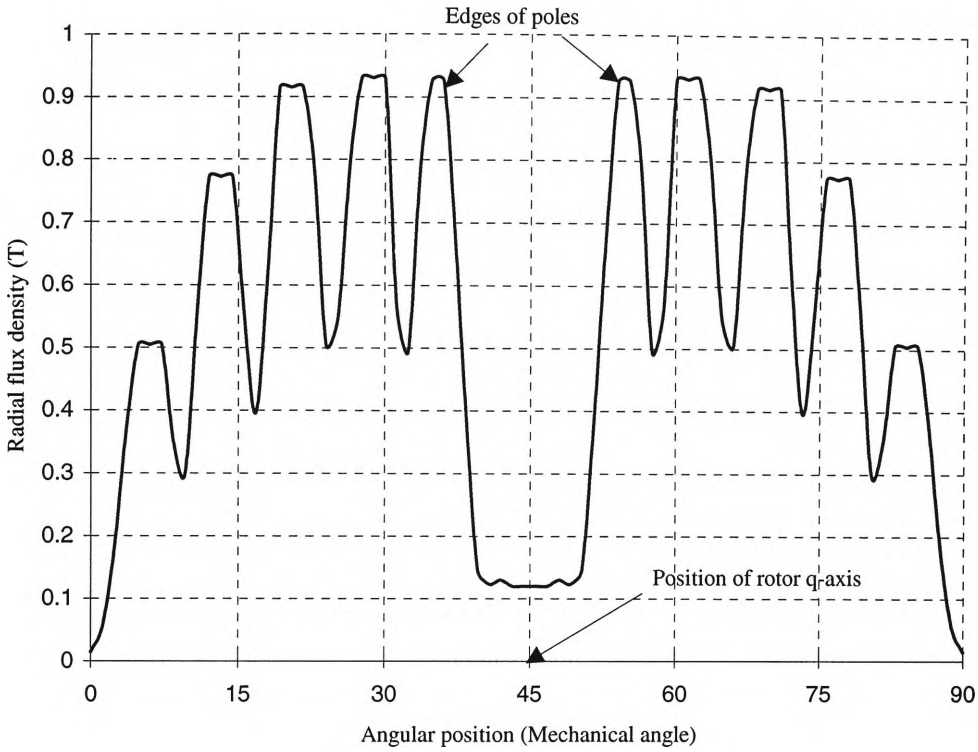

Figure 6.3 Radial component of airgap flux density wave for a uniform airgap machine

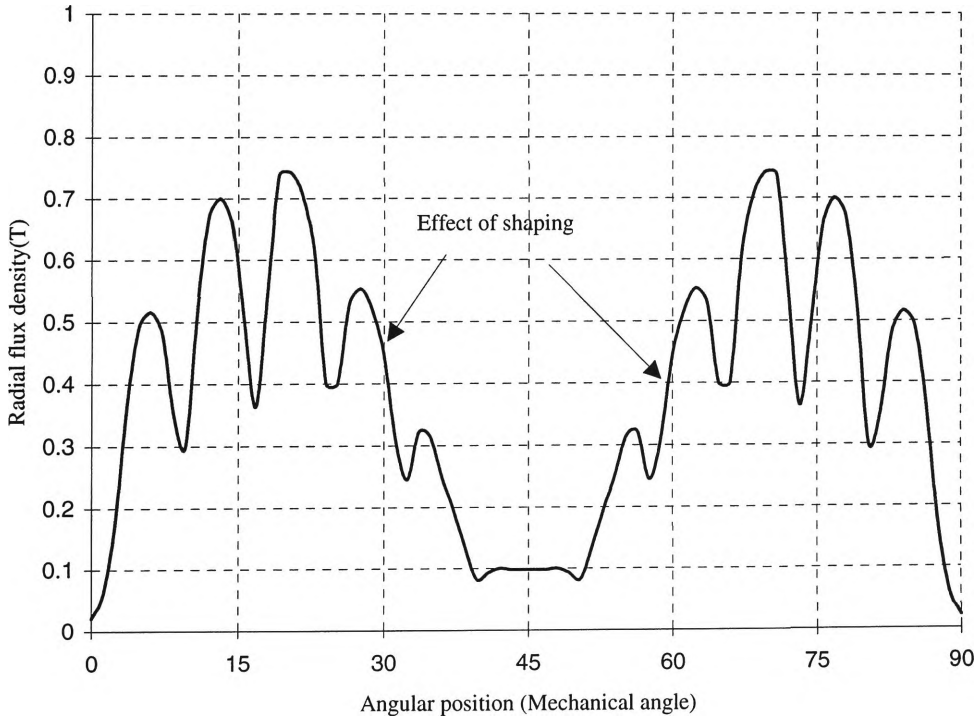

Figure 6.4 Radial component of airgap flux density wave for a shaped airgap machine

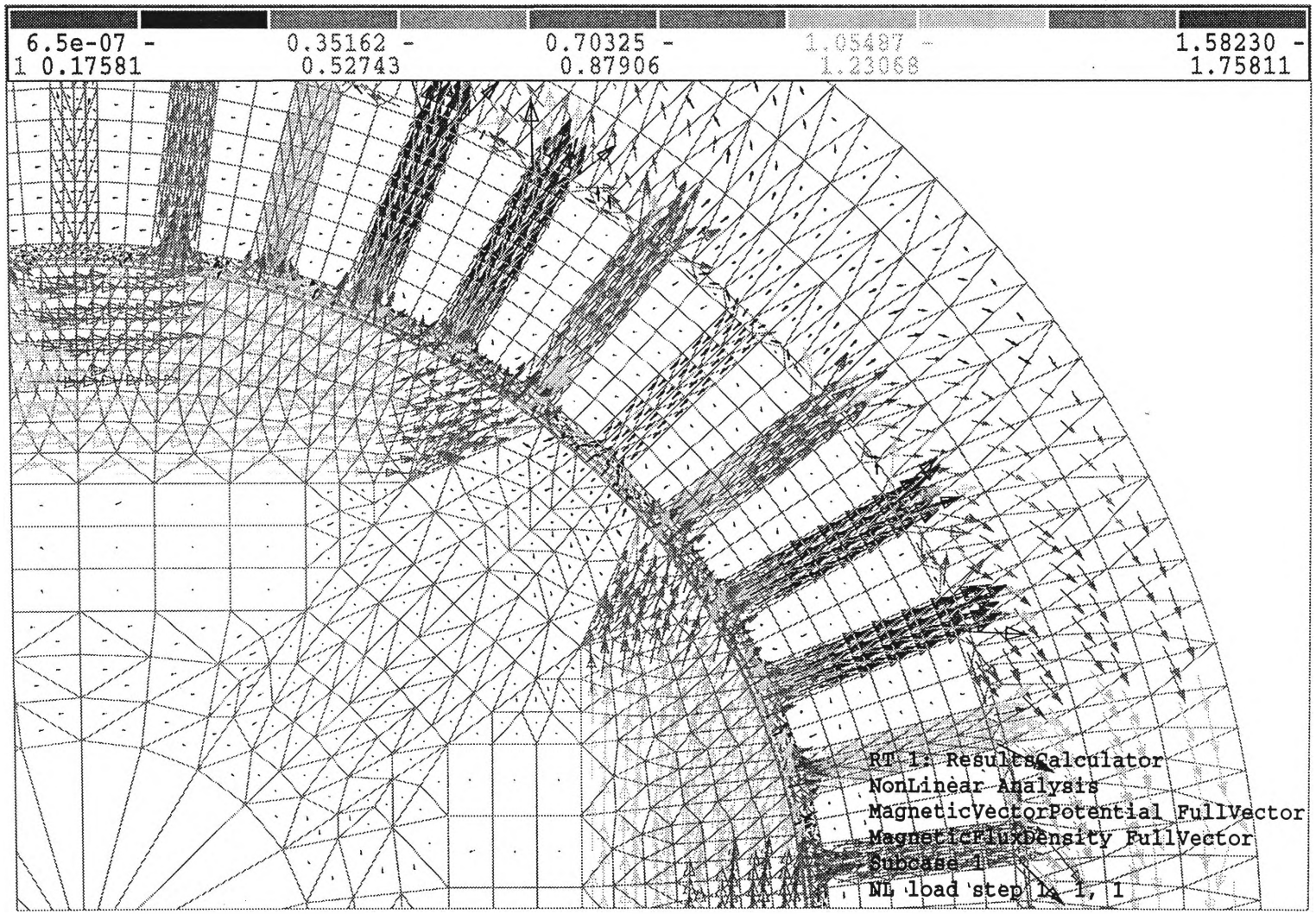

Figure 6.5 Arrow plot of full vector component of flux density distribution for the uniform airgap machine

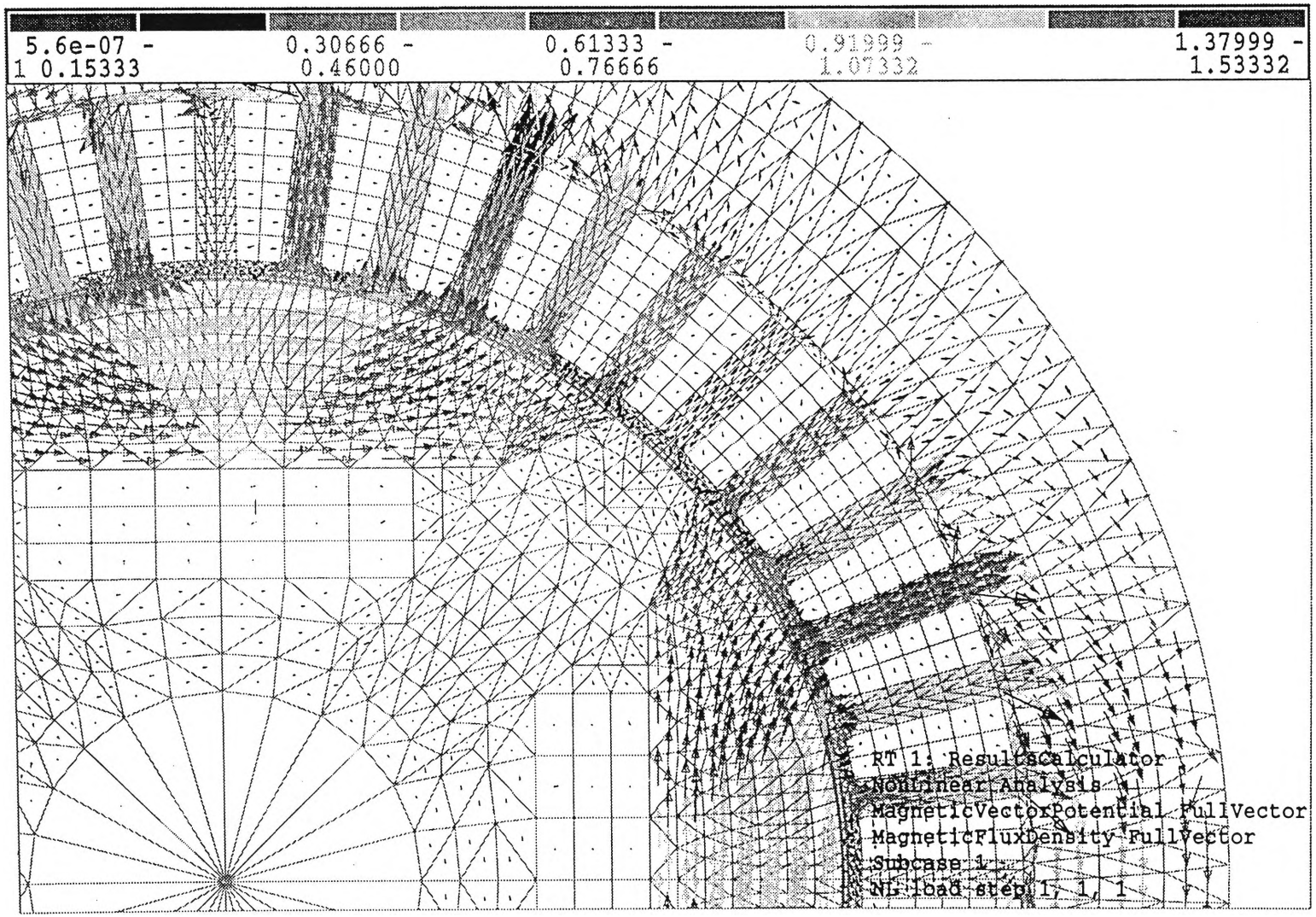

Figure 6.6 Arrow plot of full vector component of flux density distribution for the shaped airgap machine

6.4 Comparison of theoretical and finite element simulation results

The values of q-axis inductance for both uniform and shaped airgap machines were calculated using the mathematical model and finite element model. The comparison of the results is shown in Table 6.3. In Table 6.3, the two rows shows the values of q-axis inductance at a particular pole arc angle of 154°. When analyzing the results obtained from the mathematical model, it can be seen that there is a reduction of about 45% in the quadrature axis inductance for the shaped airgap machine when compared to the uniform airgap machine. The percentage reduction between the shaped and uniform airgap machine from finite element model is around 33%. The difference in the percentage reduction between the two results can be attributed to the assumptions that are used in the mathematical model. The mathematical model uses a hypothetical winding distribution spread over the full pole arc angle. The finite element model uses the discrete windings that are distributed in the stator slots. From Table 6.3, it can also be seen that there is a good agreement between the results obtained from theoretical and finite element models.

Method of calculation	Uniform airgap machine L_q (H)	Shaped airgap machine L_q (H)
Mathematical model (Hypothetical winding distribution)	0.1066	0.0584
Finite element model (Discrete winding)	0.0931	0.0623

Table 6.3 Quadrature axis inductances

6.5 Summary

The application of mathematical models and finite element models to a 5.5kW standard frame size prototype machine was presented in this chapter. The q-axis inductance for both uniform and shaped airgap machines are also compared in this chapter. The q-axis inductance calculated from mathematical model and finite element models is found to be in good agreement.

CHAPTER 7

CONCLUSIONS AND FUTURE DIRECTIONS

7.1 Conclusions

One of the important aspects in the motor design is the theoretical estimation of relevant motor design parameters. The ability to optimally select the design parameters of a particular machine to meet the given operating requirements and constraints is also of significant importance in the motor design. The work presented in this thesis is aimed at the design and optimization of an interior permanent magnet (IPM) synchronous motor. In this project, emphasis is placed on reducing the quadrature axis inductance, by means of which better vector control and faster dynamics of the machine can be obtained, while maintaining a highest possible torque/ampere ratio for a given frame size of the motor. A general mathematical model of the IPM motor is developed and the optimum dimensions of the magnetic circuit of the rotor is determined. It was shown that the q-axis inductance of the shaped airgap machine is less in comparison with the q-axis inductance of the uniform airgap machine. Substantial reduction of the q-axis inductance is achieved by the pole shaping process. In vector control of the machines, the reduced quadrature axis inductance would be a major advantage as the quadrature axis current can be controlled quickly making the machine fast responding. These mathematical models are applied to two prototype machines. The results obtained from the mathematical models of the IPM motor are further checked against the results from finite element analysis. It was found that there is a good agreement between the results from the developed mathematical models and finite element models.

7.2 Recommendations for future work

The 5.5kW prototype machine having a shaped airgap profile has to be fabricated and tested to verify the results presented in this thesis. Further

investigations are required to establish the level of torque pulsations exhibited by the machine when vector control is applied. A suitable vector controlled drive system has to be designed, built and tested to evaluate the steady state and dynamic performance of the machine.

A general theoretical relationship between the magnet volume and the torque characteristics of the shaped airgap machine can be established. This relation can further be tested by using finite element analysis.

Further investigations may be also be carried out to examine the temperature effects on the interior permanent magnet motor having a shaped airgap profile.

AUTHOR'S PUBLICATIONS

[1] Sriram, N., and Perera, B.S.P., *'Design optimization of an interior permanent magnet motor: Mathematical and finite element modelling'*, AUPEC'97, Australian Universities Power Engineering Conference, Sept. 1997 (submitted for review).

BIBLIOGRAPHY

[1] Gordon, R. Slemon, *Electric machines and drives*, Addison-Wesley Publishing Company, 1980.

[2] Longya Xu, Lurong Ye, Li Zhen and Ahmed El-Antably, '*A new design concept of permanent magnet machine for flux weakening operation*', IEEE Trans. Ind. Appl., Vol. 31, No. 2, Mar/Apr 1995, pp. 373-378.

[3] Binns, K.J., '*Permanent magnet motors for inverter fed drives*', Proc. of the conference on drives/motors/controls 84, 24-26 Oct 1994, Brighton, pp. 101-105.

[4] Binns, K.J., Barnard, W.R., and Jabbar, M.A., '*Hybrid permanent magnet synchronous motors*', Proc. IEE, Vol. 125, No. 3, Mar 1978, pp. 203-208.

[5] Weinmann, D., Nicoud, G., and Gallo, F., '*Advantages of permanent magnet motors*', Proc. of the conference on drives/motors/controls 84, 24-26 Oct 1994, Brighton, pp. 113-120.

[6] Binns, K.J., and Wong, T.M., '*Analysis and performance of a high field permanent magnet synchronous machine*', IEE Proc., Vol. 131, No. 6, Nov 1984, pp. 252-258.

[7] Low, T.S., Binns, K.J., Rahman, M.F., and Wee, L.B., '*A Nd-Fe-B permanent magnet motor Design and Performance*', Third International Conference on Electrical Machines and Drives, Conf. Publ. No. 282, 16-18 Nov 1987, pp. 246-249.

[8] Siemens, *An electric machine having permanent magnets mounted in the rotor between its pole segments*, British patent 1177247.

[9] Hippner, M., and Harley, R.G., '*Looking for an optimal rotor for high speed permanent magnet synchronous machine*', IEEE/IAS '92 Annual meeting conf. Record, Oct 1992, pp. 265-270.

[10] Islam, F., '*An Interior permanent magnet machine with shaped poles*', ME (Hons.), Thesis, University of Wollongong, 1993.

[11] Sneyers, B., Novotny, D., and Lipo, T.A., '*Field weakening in buried permanent magnet AC motor drives*', IEEE Trans., 1985, IA-21, pp. 398-407.

[12] Jahns, T.M., '*Flux weakening regime operation of an interior permanent magnet synchronous motor drive*', IEEE Trans., 1987, IA-23, pp. 681-689.

[13] Sebastian, T., and Slemon, G.R., '*Operating limits of inverter driven permanent magnet motor drives*', IEEE Trans., 1987, IA-23, pp. 327-333.

[14] Schifferl, R.F., and Lipo, T.A., '*Power capability of salient pole permanent magnet synchronous motor in variable speed drive applications*', IEEE Trans., 1990, IA-26, pp. 115-123.

[15] Soong, W.L., and Miller, T.J.E., '*Field weakening performance of brushless synchronous AC motor drives*', IEE Proc. Electrical Power appl., Vol. 141, No. 6, Nov 1994, pp. 331-340.

[16] Morimoto, S., Sanada, M., and Takeda, Y., '*Effects and compensation of magnetic saturation in flux weakening controlled permanent magnet synchronous motor drives*', IEEE Trans. on Ind. Appl., Vol. 30, No. 6, Nov-Dec 1994, pp. 1632-1637.

[17] Jang-Mok Kim, Kitae Park, Seog-Joo Kang, Seung-Ki Sul, and Jung-Lock Kwon, '*Improved dynamic performance of interior permanent magnet synchronous motor drive for flux weakening operation*', PESC 96, Record. 27th Annual IEEE Power Electronics Specialists Conference, Vol. 2, 1996, pp. 1562-1567.

[18] Zeng, Zhaohui Zhou, E., and Liang, D.T.W., '*New flux weakening control algorithm for interior permanent magnet synchronous motors*', Iecon Proc. (Industrial Electronics Conference), Vol. 2, 1996, pp. 1183-1186.

[19] Kim, J.M., and Sul, S.K., '*Speed control of interior permanent magnet synchronous motor drives for the flux weakening operation*', IEEE Trans. on Ind. Appl., Vol. 33, No. 1, Jan-Feb 1997, pp. 43-48.

[20] Schiferl, R., and Lipo, T.A., '*Core loss in buried magnet permanent magnet synchronous motors*', IEEE Tranc. on Energy conversion, Vol. 4, No. 2, Jun 1989, pp. 279-284.

[21] Vaez, S., and John, V.I., '*Minimum loss operation of PM motor drives*', Canadian Conference on Electrical and Computer Engineering, IEEE, Vol. 1, 1995, pp.284-287.

[22] Ojo, O., and Cox, J., '*Investigation into the performance characteristics of an interior permanent magnet generator including saturation effects*', Conference record - IAS Annual meeting, IEEE, Vol. 1, 1996, pp. 533-540.

[23] Consoli, A., and Renna, G., '*Interior type permanent magnet synchronous motor analysis by equivalent circuits*', IEEE Trans. on Energy conversion, Vol. 4, No. 4, Dec 1989, pp. 681-689.

[24] Nady Boules, '*Design optimization of permanent magnet DC motors*', IEEE Trans. on Ind. Applications, Vol. 26, No. 4, Jul/Aug 1990, pp. 786-792.

[25] Arkadan, A.A., Subramaniam-Sivanesan, and Demersdash, N.A.O., '*Shape optimization of PM devices using constrained gradient based inverse problem methodology*', IEEE Trans. on magnetics, Vol. 32, No. 3, May 1996, pp. 1222-1225.

[26] Il-han Park, '*Design sensitivity analysis for transient eddy current problems using finite element discretization and adjoint variable method*', IEEE Trans. on magnetics, Vol. 32, No. 3, May 1996, pp. 1242-1245.

[27] Morimoto Shigeo, Sanada Masayuki, Takeda Yoji, and Taniguchi Katsunori, '*Optimum machine parameters and design of inverter-driven synchronous motors for wide constant power operation*', Conference record-IAS annual meeting, IEEE, Vol. 1, 1994, pp. 177-182.

[28] Sim, D.J., Cho, D.H., Chun, J.S., Jung, H.K., and Chung, T.K., '*Efficiency optimization of interior permanent magnet synchronous motor using genetic algorithms*', IEEE Trans. on Magnetics, Vol. 33, Part 2, Mar 1997, pp. 1880-1883.

[29] Peter Campbell, *Permanent magnet materials and their application*, Cambridge University Press, Cambridge, 1994.

[30] Hanselman, D.C., *Brushless permanent magnet motor design*, McGraw Hill, Inc., 1994.

[31] Sheppard, J. Salon, *Finite element analysis of electrical machines*, Kluwer academic Publishers, 1995.

[32] McCaig, M., '*Energy relations in hard and soft magnet materials*', IEEE Trans. Power Electronics, Vol. 5, No. 2, Apr 1990, pp. 133-139.

[33] Slemon, G.R., '*Electrical machines for variable frequency drives*', Proc. IEEE, Vol. 82, No. 8, Aug 1994, pp. 1129-39.

[34] Jahns, T.M., Kilman, G.B., and Neumann, T.W., '*Interior PM synchronous motors for adjustable-speed drives*', IEEE Trans. Ind. Appl., Vol. IA-22, No. 4, Jul/Aug 1986, pp. 738-747.

[35] Soong, W.L., Staton, D.A., and Miller, T.J.E., '*Design of a new axially-laminated interior permanent magnet motor*', IEEE Trans. Ind. Appl., Mar/Apr 1995, pp. 358-67.

[36] Randass, G.T., and Subramanium, V., '*Evaluation of control methods for permanent magnet synchronous motors*', Proc. Inter. Conf. Power Electronics, Vol. 1, Cat. No. 95TH8025, 1995, pp. 303-8.

[37] Sebastian, T., and Slemon, G.R., '*Performance and design of permanent magnet AC motor drives*', IEEE Ind. Appl. Society, Tutorial course, 1991, pp. 2.1-2.37.

[38] Morimoto, S., Tong, Y., and Hirasa, T., '*Loss minimization control of permannet magnet synchronous motor drives*', IEEE Trans. Ind. Electronics, Vol. 41, Oct 1994, pp. 511-17.

[39] Morimoto, S., Takeda, Y., and Hirasa, T., '*Current phase control methods for permanent magnet synchronous motors*', IEEE Trans. Power Electronics, Vol. 5, No. 2, Apr 1990, pp. 133-139.

[40] Shigeo Morimotto, Masayuki Sanada, and Yoji Takeda, '*Inverter-driven synchronous motors for constant power*', IEEE Ind. Appl. Magazine, Vol. 2, No. 6, Nov/Dec 1996, pp. 18-24.

[41] Vas, P., *Vector control of AC machines*, Clarendon press, Oxford, 1990.

[42] Jahns, J.M., '*Motion control with permanent magnet AC machines*', Proc. IEEE, Vol. 82, No. 8, Aug 1994, pp. 1241-52.

[43] Merle, R., Diop, A., and Binesti, D., '*Permanent magnet operating conditions in some electrical machines. Influence of the field intensity and angle*', IEEE Trans. Magnetics, Vol. 31, No. 3, May 1995, pp. 1805-1808.

[44] Sebastian, T., '*Temperature effects on torque production and efficiency of PM motors using Nd-Fe-B magnets*', IEEE Trans. Ind. Appl., Vol. 31, No. 2, Mar/apr 1995, pp. 353-357.

[45] Sarma Mulukutla, S., *Electric machines : Steady state theory and dynamic performance*, WM.C. Brown Publishers: Dubuque, Iowa, 1985, pp.73-80.

[46] Nady Boules, '*Prediction of no-load flux density distribution in permanent magnet machines*', IEEE Trans. Ind. Appl., Vol. IA-21, No. 4, May/Jun 1985, pp. 633-643.

[47] Mellor, P.H., Chaaban, E.B., and Binns, K.J., '*Estimation of parameters and performance of rare-earth permanent magnet motors avoiding measurement of load angle*', IEE Proc., Vol. 138, Pt. B, No. 6, Nov 1991, pp.322-330.

[48] Chari, M.V.K., and Silvester, P.P., *Finite elements in Electrical and magnetic field problems*, Chichester, New York, John Willey and Sons, 1980.

[49] Rahman, M.A., and Zhou, P., '*Finite element analysis of line start permanent magnet synchronous motors*', Conference on Industrial drives, Rockhampton, Australia, 18-20 Sep 1991, pp. 278-283.

[50] Iskander magdy, F., *'Electromagnetics fields and waves'*, Prentice Hall, 1992.

[51] Clarence, N., Obiozor, and Matthew, N.O. Sadilu, *'Finite elements in electromagnetics for undergraduate curriculum'*, Proc. Of IEEE Southeast con '93, Cat. No. 93CH3295-3, 1993, pp. 684-687.

[52] Zienkiewicz, O.C., and Taylor, R.L., *The finite element method*, 4th edition, McGraw-Hill, 1989.

[53] The MacNeal -Schwendler Corporation : *MSC/XL User's manual*, Version 3B, USA, 1992.

[54] Li, T., and Slemon, G., *'Reduction of cogging torque in permanent magnet motors'*, IEEE Trans. Magnetics, Vol. 24, No. 6, Nov 1988, pp. 2901-2903.

APPENDIX A

Calculation of airgap length for the existing prototype machine

Table A1 shows the calculated values of the airgap lengths of the shaped airgap machine at different angles, measured from rotor d-axis. The prototype machine has a minimum airgap length of 0.838mm and radius of the stator (R) equal to 65.0875 mm.

Mechanical angle (deg)	Airgap length from Equ.(2.8) mm	Radius of the rotor (Rr) mm	Airgap (R - Rr) mm
0.00	0.8380	64.2495	0.8380
1.25	0.8388	64.2495	0.8380
2.50	0.8412	64.2475	0.8400
3.75	0.8452	64.2435	0.8440
5.00	0.8509	64.2382	0.8493
6.25	0.8583	64.2301	0.8574
7.50	0.8676	64.2218	0.8657
8.75	0.8787	64.2097	0.8778
10.00	0.8918	64.1973	0.8902
11.25	0.9070	64.1819	0.9056
12.50	0.9246	64.1646	0.9229
13.75	0.9447	64.1439	0.9436
15.00	0.9676	64.1221	0.9654
16.25	0.9936	64.0962	0.9913
17.50	1.0230	64.0656	1.0219
18.75	1.0563	64.0330	1.0545
20.00	1.0939	63.9945	1.0930
21.25	1.1366	63.9531	1.1344
22.50	1.1851	63.9039	1.1836
23.75	1.2404	63.8503	1.2372
25.00	1.3037	63.7863	1.3012
26.25	1.3766	63.7123	1.3752
27.50	1.4610	63.6295	1.4580
28.75	1.5597	63.5325	1.5550
30.00	1.6760	63.4160	1.6715
31.25	1.8148	63.2763	1.8112
32.50	1.9829	63.1050	1.9825
33.75	2.1898	62.8977	2.1898
35.00	2.4501	62.6420	2.4455
36.25	2.7868	62.3066	2.7809
37.50	3.2378	61.8479	3.2396
38.75	3.8717	61.5020	3.5855

Table A1 Air gap lengths at different pole arc angles

APPENDIX B

Specifications of the existing prototype machine

Axial length of stator core	=	77 mm
Number of slots	=	36
Number of slots per pole per phase	=	3
Number of poles	=	4
Number of winding layers	=	2
Number of turns in a coil	=	18
Coil pitch	=	7 slots
Rated peak value of sinusoidal phase current	=	6 A/phase
Radius of the rotor	=	65.0875 mm
Minimum length of the airgap	=	0.838 mm
Rotor pole arc angle	=	154°
Open circuit voltage (@1500 rpm)	=	240V(L-L).

APPENDIX C

Calculation of hypothetical stator winding distribution

The number of turns present in the hypothetical stator winding distribution that is employed in the finite element model of the machine are calculated using the expression in Equation (2.10) of Chapter 2. The turns distribution of hypothetical stator windings spread over the pole arc angle of 180° and the squeezed stator windings are shown in Table C1.

Mechanical angle (deg)	Number of turns spread over the full pole arc angle	Number of turns for a squeezed winding distribution
0	62.00	75.40
1	61.96	75.33
2	61.85	75.13
3	61.66	74.79
4	61.40	74.32
5	61.06	73.71
6	60.65	72.97
7	60.16	72.09
8	59.60	71.09
9	58.97	69.96
10	58.26	68.71
11	57.49	67.33
12	56.64	65.83
13	55.73	64.21
14	54.74	62.47
15	53.69	60.62
16	52.58	58.66
17	51.40	56.60
18	50.16	54.44
19	48.86	52.17
20	47.49	49.81
21	46.07	47.37
22	44.60	44.84
23	43.07	42.22
24	41.49	39.53
25	39.85	36.77
26	38.17	33.95
27	36.44	31.06
28	34.67	28.11
29	32.85	25.12
30	31.00	22.08
31	29.11	19.00
32	27.18	15.89
33	25.22	12.74
34	23.23	9.58
35	21.21	6.39
36	19.16	3.20
37	17.09	0.00
38	15.00	0.00
39	12.89	0.00
40	10.77	0.00
41	8.63	0.00
42	6.48	0.00
43	4.32	0.00
44	2.16	0.00

Table C1 Turns distribution of hypothetical windings spread over full pole arc angle and squeezed hypothetical stator windings

APPENDIX D

Calculation of q-axis inductances

The calculation of q-axis inductance of the machine can be carried out by determining the flux linkage which is given by the product of number of turns linking the flux. Table D1 shows the calculated value of the q-axis inductance for the uniform airgap machine having a hypothetical stator winding spread over the full pole arc angle. The value of q-axis inductance is found to be equal to 0.0477H. Table D2 shows the calculated value of the q-axis inductance for the uniform airgap machine having squeezed hypothetical stator windings. The value of q-axis inductance is found to be equal to 0.0659H. Table D3 shows the calculated value of the q-axis inductance for the shaped airgap machine having squeezed hypothetical stator windings. The value of q-axis inductance is found to be equal to 0.0385H.

Mechanical angle (deg)	flux density (T)	Number of turns	flux linkage (Wb-turns)
0	0.00730	62.00	0.000006
1	0.01792	61.95	0.000027
2	0.02977	61.84	0.000067
3	0.04185	61.66	0.000126
4	0.05363	61.40	0.000202
5	0.06577	61.05	0.000297
6	0.07711	60.65	0.000405
7	0.08881	60.16	0.000532
8	0.10030	59.60	0.000673
9	0.11164	58.97	0.000830
10	0.12300	58.26	0.001001
11	0.13420	57.49	0.001187
12	0.14500	56.64	0.001382
13	0.15607	55.73	0.001594
14	0.16700	54.74	0.001817
15	0.17700	53.69	0.002042
16	0.18741	52.58	0.002282
17	0.19740	51.40	0.002528
18	0.20700	50.16	0.002777
19	0.21680	48.86	0.003038
20	0.22610	47.50	0.003299
21	0.23490	46.08	0.003560
22	0.24380	44.60	0.003827
23	0.25218	43.07	0.004091
24	0.26040	41.49	0.004356
25	0.26830	39.85	0.004619
26	0.27587	38.17	0.004878
27	0.28285	36.44	0.005127
28	0.28970	34.67	0.005373
29	0.29640	32.86	0.005616
30	0.30230	31.00	0.005842
31	0.30825	29.11	0.006067
32	0.31370	27.18	0.006278
33	0.31870	25.22	0.006476
34	0.32340	23.23	0.006663
35	0.32760	21.21	0.006835
36	0.33151	19.16	0.006994
37	0.33510	17.09	0.007139
38	0.33760	14.99	0.007254
39	0.30300	12.89	0.006558
40	0.18000	10.77	0.003920
41	0.09300	8.63	0.002035
42	0.06250	6.48	0.001373
43	0.05000	4.32	0.001101
44	0.04610	2.10	0.001016
		Inductance	0.0477

Table D1 Calculation of q-axis inductance for uniform airgap machine having hypothetical stator winding distribution

Mechanical angle (deg)	flux density (T)	Number of turns	flux linkage (Wb-turns)
0	0.01630	75.40	0.000015
1	0.02650	75.33	0.000049
2	0.04400	75.13	0.000121
3	0.06100	74.79	0.000224
4	0.07877	74.32	0.000360
5	0.09590	73.71	0.000525
6	0.11300	72.97	0.000719
7	0.13000	72.09	0.000941
8	0.14690	71.09	0.001191
9	0.16290	69.96	0.001460
10	0.17930	68.71	0.001757
11	0.19520	67.33	0.002073
12	0.21050	65.83	0.002405
13	0.22585	64.21	0.002757
14	0.24050	62.47	0.003119
15	0.25500	60.62	0.003496
16	0.26888	58.66	0.003878
17	0.28230	56.60	0.004267
18	0.29520	54.44	0.004658
19	0.30760	52.17	0.005049
20	0.31960	49.81	0.005440
21	0.33080	47.37	0.005822
22	0.34162	44.84	0.006199
23	0.35170	42.22	0.006563
24	0.36140	39.53	0.006919
25	0.37010	36.77	0.007251
26	0.37845	33.95	0.007572
27	0.38600	31.06	0.007869
28	0.39290	28.11	0.008144
29	0.39910	25.12	0.008395
30	0.40450	22.08	0.008617
31	0.40900	19.00	0.008808
32	0.41340	15.89	0.008983
33	0.41670	12.74	0.009119
34	0.41930	9.58	0.009225
35	0.42293	6.39	0.009338
36	0.42110	3.20	0.009314
37	0.36550	0.00	0.008084
38	0.25600	0.00	0.005662
39	0.17100	0.00	0.003782
40	0.10900	0.00	0.002411
41	0.07300	0.00	0.001615
42	0.06000	0.00	0.001327
43	0.05230	0.00	0.001157
44	0.04900	0.00	0.001084
		Inductance	0.0659

Table D2 Calculation of q-axis inductance for uniform airgap machine having squeezed hypothetical stator winding distribution

Mechanical angle (deg)	flux density (T)	Number of turns	flux linkage (Wb-turns)
0	0.01200	75.40	0.000006
1	0.02750	75.33	0.000025
2	0.04450	75.13	0.000061
3	0.06090	74.79	0.000112
4	0.07971	74.32	0.000182
5	0.09655	73.71	0.000264
6	0.11290	72.97	0.000359
7	0.12760	72.09	0.000462
8	0.14200	71.09	0.000576
9	0.15660	69.96	0.000702
10	0.17075	68.71	0.000837
11	0.18310	67.33	0.000972
12	0.19420	65.83	0.001109
13	0.20436	64.21	0.001247
14	0.21400	62.47	0.001388
15	0.22270	60.62	0.001526
16	0.22810	58.66	0.001645
17	0.23517	56.60	0.001777
18	0.23900	54.44	0.001886
19	0.24340	52.17	0.001998
20	0.24553	49.81	0.002090
21	0.24620	47.37	0.002167
22	0.24576	44.84	0.002230
23	0.24398	42.22	0.002277
24	0.24118	39.53	0.002309
25	0.23600	36.77	0.002312
26	0.23130	33.95	0.002314
27	0.22400	31.06	0.002283
28	0.21740	28.11	0.002253
29	0.20860	25.12	0.002194
30	0.19910	22.08	0.002121
31	0.18820	19.00	0.002027
32	0.17666	15.89	0.001919
33	0.16466	12.74	0.001802
34	0.15120	9.58	0.001663
35	0.13780	6.39	0.001521
36	0.12311	3.20	0.001362
37	0.10700	0.00	0.001183
38	0.09100	0.00	0.001006
39	0.07600	0.00	0.000841
40	0.06400	0.00	0.000708
41	0.05476	0.00	0.000606
42	0.04800	0.00	0.000531
43	0.04470	0.00	0.000494
44	0.04200	0.00	0.000464
		Inductance	0.0385

Table D3 Calculation of q-axis inductance for shaped airgap machine having squeezed hypothetical stator winding distribution

APPENDIX E

Specifications of the 5.5kW prototype machine

Stator details of uniform airgap and shaped airgap machines:

Axial length of stator core	=	85 mm
Number of slots	=	48
Number of slots per pole per phase	=	4
Number of poles	=	4
Number of winding layers	=	2
Number of turns in a coil	=	15
Coil pitch (in slots)	=	10 slots
Inner radius of the stator	=	71.505 mm
Outer radius of the stator	=	115 mm
Open circuit voltage (@ 1500 rpm)	=	240V(L-L)
Rated peak value of phase current	=	11A/phase

Stator slot dimensions in mm are given in Figure E1.

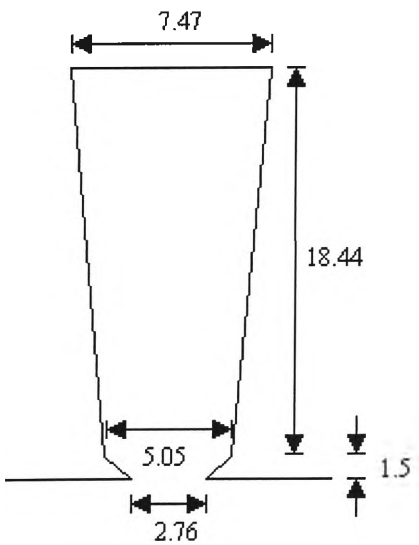

Figure E1 Stator slot dimensions

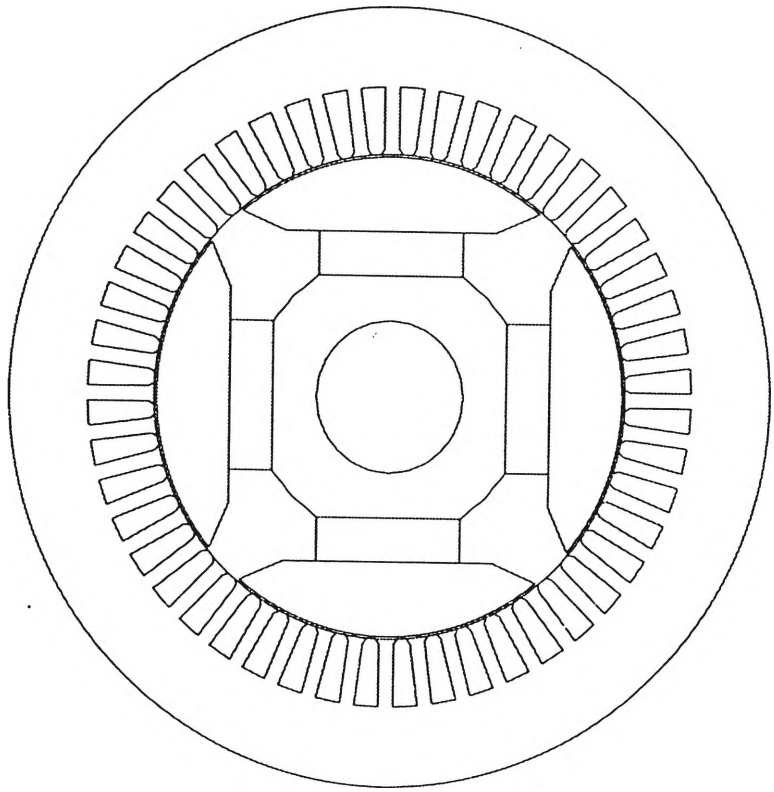

Figure E2 Geometry of uniform airgap machine

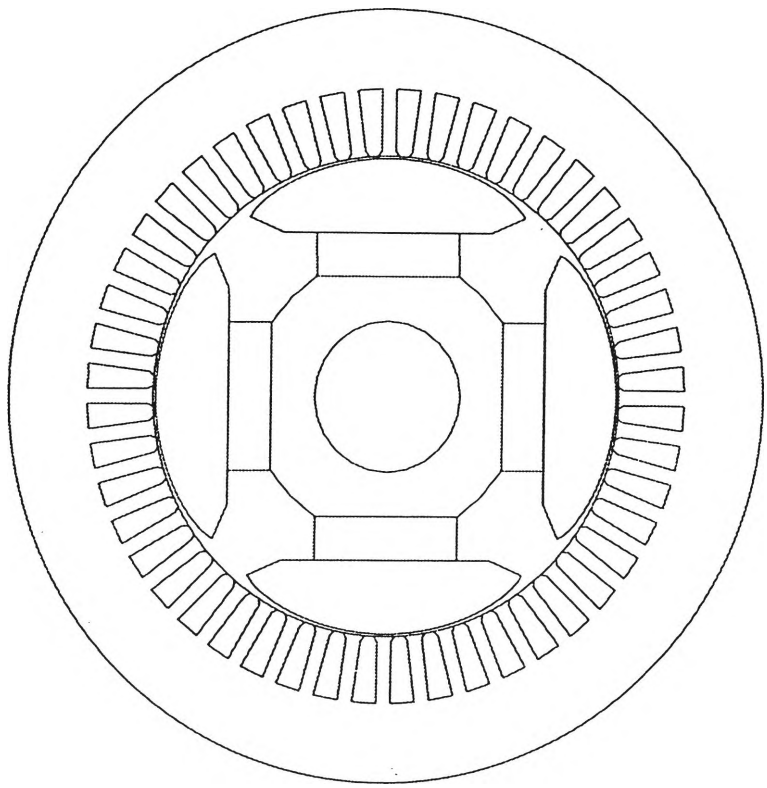

Figure E3 Geometry of shaped airgap machine

APPENDIX F

Calculation of shaped airgap length for the 5.5kW prototype machine

Table F1 gives the calculated values of shaped airgap lengths at different pole arc angles employed using the Equation (2.8) of Chapter 2.

Mechanical angle (deg)	Airgap from Equ.(2.8) mm	Radius of the rotor (Rr) mm
0.00	0.8050	70.7000
1.25	0.8058	70.6992
2.50	0.8081	70.6969
3.75	0.8119	70.6931
5.00	0.8174	70.6876
6.25	0.8245	70.6805
7.50	0.8334	70.6716
8.75	0.8441	70.6609
10.00	0.8567	70.6483
11.25	0.8713	70.6337
12.50	0.8882	70.6168
13.75	0.9075	70.5975
15.00	0.9295	70.5755
16.25	0.9545	70.5505
17.50	0.9827	70.5223
18.75	1.0147	70.4903
20.00	1.0509	70.4541
21.25	1.0919	70.4131
22.50	1.1384	70.3666
23.75	1.1916	70.3134
25.00	1.2524	70.2526
26.25	1.3224	70.1826
27.50	1.4035	70.1015
28.75	1.4982	70.0068
30.00	1.6100	69.8950
31.25	1.7434	69.7616
32.50	1.9048	69.6002
33.75	2.1036	69.4014
35.00	2.3537	69.1513
36.25	2.6770	68.8280
37.50	3.1103	68.3947
38.75	3.7193	67.7857

Table F1 Shaped airgap lengths at different pole arc angles